Architecture and dynamics of a desmosome–endoplasmic reticulum complex

Navaneetha Krishnan Bharathan [1], William Giang [1], Coryn L. Hoffman[1], Jesse S. Aaron [2], Satya Khuon[2], Teng-Leong Chew [2], Stephan Preibisch [2], Eric T. Trautman [2], Larissa Heinrich[2], John Bogovic [2], Davis Bennett[2], David Ackerman[2], Woohyun Park[2], Alyson Petruncio[2], Aubrey V. Weigel [2], Stephan Saalfeld[2], COSEM Project Team, A. Wayne Vogl[3], Sara N. Stahley[1] & Andrew P. Kowalczyk [1] ✉

The endoplasmic reticulum (ER) forms a dynamic network that contacts other cellular membranes to regulate stress responses, calcium signalling and lipid transfer. Here, using high-resolution volume electron microscopy, we find that the ER forms a previously unknown association with keratin intermediate filaments and desmosomal cell–cell junctions. Peripheral ER assembles into mirror image-like arrangements at desmosomes and exhibits nanometre proximity to keratin filaments and the desmosome cytoplasmic plaque. ER tubules exhibit stable associations with desmosomes, and perturbation of desmosomes or keratin filaments alters ER organization, mobility and expression of ER stress transcripts. These findings indicate that desmosomes and the keratin cytoskeleton regulate the distribution, function and dynamics of the ER network. Overall, this study reveals a previously unknown subcellular architecture defined by the structural integration of ER tubules with an epithelial intercellular junction.

The endoplasmic reticulum (ER) is the largest and perhaps most architecturally complex membranous organelle in eukaryotic cells[1]. The ER participates in protein biosynthesis and turnover, organelle biogenesis, the transfer of lipids between membranous compartments, and regulation of calcium homeostasis[2,3]. These functions are often conducted at membrane contact sites between the ER and other organelles including endosomes, mitochondria and the plasma membrane (PM)[1,2]. For these reasons, it is of particular interest to understand how the spatio-temporal behaviour of ER membranes is regulated. The morphology and dynamics of the ER have been studied predominantly in individual mammalian cells, including fibroblasts and COS-7 (refs. 4,5). However, little is known about how ER tubule organization and dynamics are coordinated between cells that form extensive cell–cell contacts.

In this Article, using cryo-fixation approaches to preserve near-native cell structure, in combination with high-resolution volume electron microscopy (EM)[6], we find that desmosomes, an adhesive cell–cell junction coupled to intermediate filament networks, organize the subcellular distribution and dynamics of ER tubules. Peripheral ER tubules follow keratin filament bundles to desmosomes where they are stabilized in mirror image-like arrangements at opposing cell–cell contacts. Disruption of desmosomes or expression of disease-causing keratin mutants alters ER morphology, dynamics and stress responses. These findings reveal the architecture of a complex at intercellular contacts comprising desmosomes, intermediate filaments and the ER. The identification of a role for desmosomes in regulating ER morphology, dynamics and stress signalling provides insights into both

[1]Departments of Dermatology and Cellular and Molecular Physiology, Pennsylvania State University College of Medicine, Hershey, PA, USA. [2]Advanced Imaging Center, Janelia Research Campus, Howard Hughes Medical Institute, Ashburn, VA, USA. [3]Life Sciences Institute and the Department of Cellular and Physiological Sciences, University of British Columbia, Vancouver, British Columbia, Canada. ✉e-mail: AndrewKowalczyk@psu.edu

fundamental organelle biology and into human disease states resulting from desmosome or keratin dysfunction.

Results

The ER associates with desmosomes

To assess the organization of ER in epithelial cells, we used A431 cell lines expressing desmoplakin (DP)-EGFP to visualize desmosomal cell–cell junctions[7] and stably transduced these cells with mApple-VAPB to visualize ER[8,9]. Confocal microscopy revealed that peripheral ER tubules associated with DP puncta on both sides of desmosomal cell–cell contacts (Extended Data Fig. 1a). Similar results were obtained using immortalized HaCaT keratinocytes and primary normal human epidermal keratinocytes (NHEKs; Extended Data Fig. 1b,c). Transmission EM of parental A431 cells lacking exogenously expressed VAPB and DP revealed that peripheral ER tubules extend towards the electron-dense desmosome plaque, often exhibiting a paired configuration on either side of the desmosomal junction. ER–desmosome associations were also readily visible in multiple epithelial tissues, including rat skin and colon (Extended Data Fig. 2).

We determined the nanoscale three-dimensional architecture of ER-desmosome associations using a cryo-structured illumination microscopy (Cryo-SIM) and focused ion beam scanning electron microscopy (FIB-SEM) workflow[6] (Supplementary Fig. 1). The cytoplasmic zone of the desmosome comprises an electron-dense outer plaque subjacent to the PM and a less electron-dense inner plaque that functions as an attachment zone for keratin intermediate filaments[10,11]. Two-dimensional views and three-dimensional reconstructions of FIB-SEM datasets revealed that peripheral ER tubules were situated close to desmosomal plaques (Fig. 1 and Supplementary Video 1). ER tubules and keratin filaments were arranged as paired structures on both sides of the desmosomal cell–cell junction (Fig. 1e–p). ER tubules were also present in the space between the keratin filament attachment zone (inner dense plaque) and the outer dense plaque of the desmosome (Extended Data Fig. 3 and Supplementary Video 2). ER tubules adjacent to desmosomes had fewer bound ribosomes relative to ER membranes further away from desmosomes (Extended Data Fig. 4). From a total of 33 desmosomes across the FIB-SEM datasets, ER tubules were found to be within 250 nm of the outer dense plaques of 94% of desmosomes ($n = 31/33$). At canonical ER–PM contact distances of 30 nm, 42% of desmosome outer dense plaques ($n = 14/33$) showed a presence of ER tubules. In 24% of desmosomes ($n = 8/33$), ER tubules were found to be in physical contact with the outer dense plaque. These data indicate that peripheral ER tubules are a previously unrecognized component of the desmosomal adhesive complex.

The ER associates with keratin filaments

Since peripheral ER tubules were observed on either side of the desmosome, we investigated ER tubule localization relative to keratin filament bundles proximal (defined hereafter as ≤250 nm) and distal (defined as >1,000 nm) to desmosomal cell–cell contacts. FIB-SEM datasets at $4 \times 4 \times 4$ nm^3 voxel size revealed that peripheral ER tubules intertwined around keratin filaments that approached the desmosome plaque (Fig. 2a,b). In addition to frequent ER–keratin contacts, keratin filament bundles were often fully enveloped by ER membrane (Fig. 2c–h and Supplementary Video 3). Keratin filaments made similar contacts with sheet-like/planar ER structures located distal to cell borders (Extended Data Fig. 4c–h and Supplementary Video 3). These observations demonstrate an intimate physical association between the ER membrane and the intermediate filament cytoskeleton.

Microtubule interactions with ER tubules have been studied extensively[12,13]. To compare ER–keratin and ER–microtubule interactions, we quantified the number and size of these contacts, defining 'contact' as a maximum distance of 16 nm between a voxel of ER and a voxel of keratin or microtubules (Extended Data Fig. 5). Within 1,000 nm of a desmosome, the ER made $n = 327$ contacts with keratin filaments and $n = 215$

contacts with microtubules (Fig. 2i). Within 250 nm, we observed substantially more ER–keratin contacts ($n = 217$) than ER–microtubule contacts ($n = 9$). Interestingly, this preference was reversed at distances >1,000 nm from a desmosome, with ER membranes making more contacts with microtubules than with keratin filaments (Extended Data Fig. 5g). Further, ER membranes made larger contacts with keratin filaments than with microtubules (Fig. 2j). These findings indicate that ER associates with both keratin filaments and microtubules, but the frequency of contact with these cytoskeletal networks differs throughout the cell.

We next sought to determine if ER tubules, like keratin filaments, are present in mirror image-like arrangements at desmosomal junctions. We analysed the distance between desmosomes and the closest voxel of ER membrane across two adjacent cells in the $4 \times 4 \times 4$ nm^3 and $8 \times 8 \times 8$ nm^3 FIB-SEM datasets, using microtubules and endosomes for comparison (Fig. 3a–d and Supplementary Video 4). We restricted our analysis to within 250 nm on either side of desmosomes that displayed radial keratin filament bundles on both cytoplasmic faces. ER membrane pairs were present across ~89% ($n = 16/18$) of desmosomes (Fig. 3e,f). In contrast, endosome pairs were present across ~22% ($n = 4/18$) of desmosomes. Reliable identification and segmentation of microtubules was possible only in the $4 \times 4 \times 4$ nm^3 dataset, where we found no microtubule pairs within 250 nm of any desmosome. These data demonstrate a symmetry in desmosome organization defined by the presence of both keratin filaments and ER tubules at desmosomal cell–cell contacts.

Peripheral ER tubules stably anchor to desmosomes

ER association with various organelles influences ER tubule mobility[5,14]. To determine if desmosomes influence ER dynamics, we used spinning disk confocal microscopy of living A431 cell lines stably expressing DP-EGFP and mApple-VAPB. ER tubules were present at the cell periphery and closely associated with virtually all desmosomes (Fig. 4a and Supplementary Video 5). Kymographs revealed that these ER-desmosome associations were highly stable (Fig. 4b). Approximately 73% of desmosomes ($n = 113/154$) co-localized with ER tubules for the entirety of a 2 min time course, while the remaining ~27% of desmosomes ($n = 41/154$) showed frequent but transient interactions with ER tubules (Fig. 4c and Extended Data Fig. 6).

To assess further how ER membrane mobility is impacted by desmosome associations, we used a membrane displacement analysis (MDA) macro in Fiji[14] to classify ER membrane into static and mobile fractions. If the ER membrane moved >2 pixels (>130 nm) between timepoints, we classified it as mobile ER. We drew regions of interest (ROIs) that either encompassed ER tubules anchored to desmosomes (desmosomal ER) (Fig. 4d) or ER tubules further away from cell–cell contacts (non-desmosomal ER) (Fig. 4e). MDA revealed that about 66% of ER membrane present at desmosomes was stable, whereas only 39% of non-desmosomal ER was stable (Fig. 4d–f). These results indicate that ER tubules associated with desmosomes are immobile relative to non-desmosomal ER tubules.

Microtubule depolymerization causes ER tubule collapse into sheets and ER retraction from the cell periphery[13]. To determine if ER anchorage to desmosomes is affected by depolymerizing the microtubule cytoskeleton, we labelled microtubules in DP-EGFP/mApple-VAPB A431 cells with Tubulin Tracker Deep Red (TTDR) and imaged living cells treated with either dimethyl sulfoxide (DMSO) or the microtubule-depolymerizing agent, nocodazole (30 μM). As microtubules depolymerized, peripheral ER tubules collapsed into a sheet-like morphology both at cell–cell borders (Fig. 5a–e) and at cell edges not contacting adjacent cells (cell-free edges) (Fig. 5f–j). In DMSO-treated cells, peripheral ER remained tubular and did not retract from the cell-free edges (Extended Data Fig. 7a). In nocodazole-treated cells, ER remained anchored to desmosomes (Fig. 5d,e (blue arrows) and Extended Data Fig. 7b) but retracted from both cell-free edges (Fig. 5g–j, Extended Data Fig. 7d and Supplementary Video 6) and
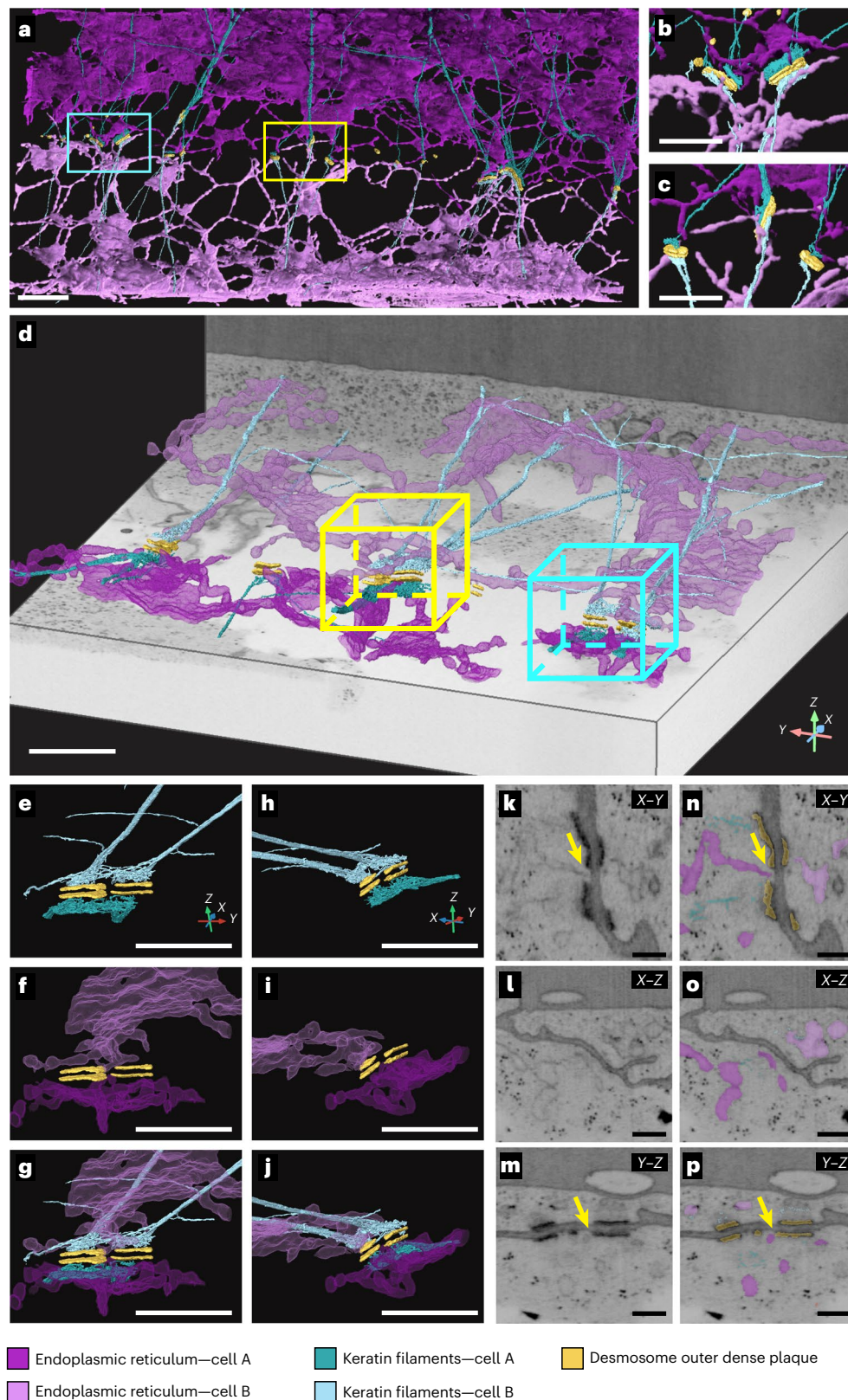
Fig. 1 | FIB-SEM reveals ER–desmosome associations. a–c, FIB-SEM segmentations of a cell–cell contact in A431 cells acquired at 8 nm isotropic voxel size showing desmosome outer dense plaques (yellow), keratin filaments (teal) and ER (magenta) (*n* = 1 cell–cell contact at 8 nm isotropic resolution). Different shades of teal and magenta distinguish keratin and ER in adjacent cells. Cyan and yellow squares indicate regions with magnified views shown in insets **b** and **c**, respectively. Scale bar, 2 μm (**a**), 1 μm (**b** and **c**). **d**, FIB-SEM segmentations of a cell–cell contact in A431 cells acquired at 4 nm isotropic voxel size (*n* = 1 cell–cell contact at 4 nm isotropic resolution). Cyan box indicates region with magnified segmentations shown in **e–j**. Yellow box is magnified in Fig. 2. Scale bar, 1 μm. **e–j**, Rotated views of a desmosome outer dense plaque (yellow) showing mirror image-like organization of teal keratin filaments (**e** and **h**) and magenta ER (**f** and **i**), and rotated views of desmosome outer dense plaque, keratin filaments and ER (**g** and **j**). Scale bar, 1 μm. **k–p**, Orthoslices in *XY* (**k** and **n**), *XZ* (**l** and **o**) and *YZ* (**m** and **p**) without or with desmosome, ER and keratin segmentations. Yellow arrows point to ER tubules proximal to desmosome outer dense plaque. Scale bar, 250 nm.
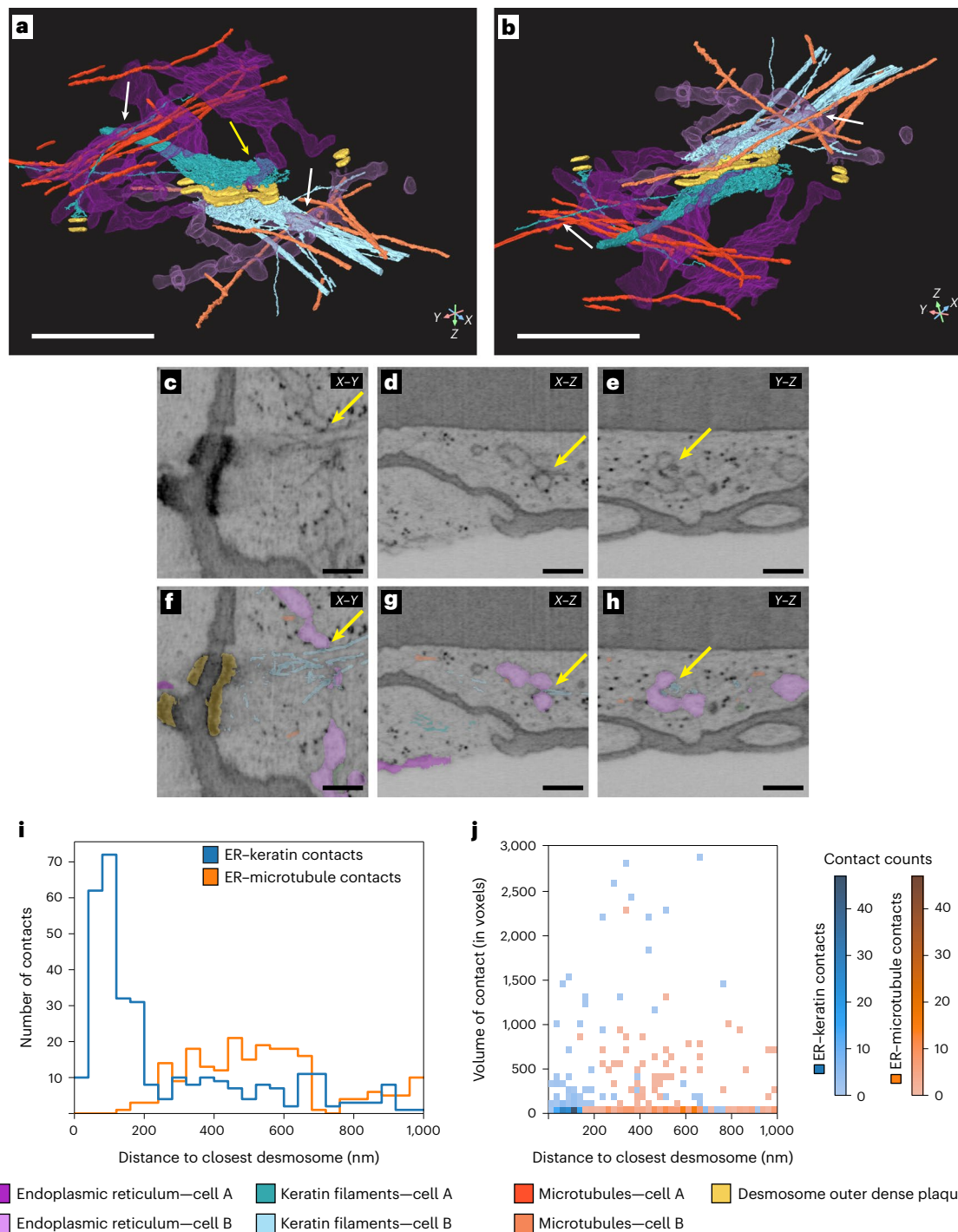
Fig. 2 | FIB-SEM reveals ER–keratin filament associations in A431 cells.
a, View of desmosome highlighted in the yellow box in Fig. 1d showing ER tubules (magenta) making contact with keratin filaments (teal; white arrow) and with the desmosome plaque (green arrow). Microtubules (orange) are also shown. **b**, Rotated views of structures shown in (**a**). Scale bar, 1 µm. **c–e**, Orthoslices showing ER tubules making contact with electron-dense keratin filaments (yellow arrows). Views along X-Y (**c**), X-Z (**d**) and Y-Z (**e**) axes. Scale bar, 250 nm. **f–h**, Same orthoslices as in **e–g** with ER, keratin and microtubule segmentations. Views along X-Y (**f**), X-Z (**g**) and Y-Z (**h**) axes. Scale bar, 250 nm. **i**, Histogram

depicting the frequency of ER–keratin (blue line) and ER–microtubule (orange line) contacts to the nearest desmosome using a contact distance threshold of 16 nm. **j**, Bivariate histogram of ER–keratin (blue) and ER–microtubule (orange) contacts showing the relationship between contact size (y-axis) and proximity to the nearest desmosome (x-axis) using a contact distance threshold of 16 nm. Colour bars depict the number of contacts with keratin (blue) or microtubules (orange). Data in **i** and **j** represent measurements from $n = 33$ desmosomes at two cell–cell contacts. Source numerical data are available in source data.

from regions of cell–cell borders lacking desmosomes (Fig. 5d,e (yellow arrows) and Extended Data Fig. 7b). Together with the data shown above (Fig. 4), these observations indicate that desmosomes function as peripheral ER-tethering sites.

ER tubules associate with remodelling desmosomes
We assessed ER–desmosome interactions as desmosomes underwent remodelling events, such as desmosomal fusion and desmosome assembly[7,15]. ER tubules remained in close association with desmosomes
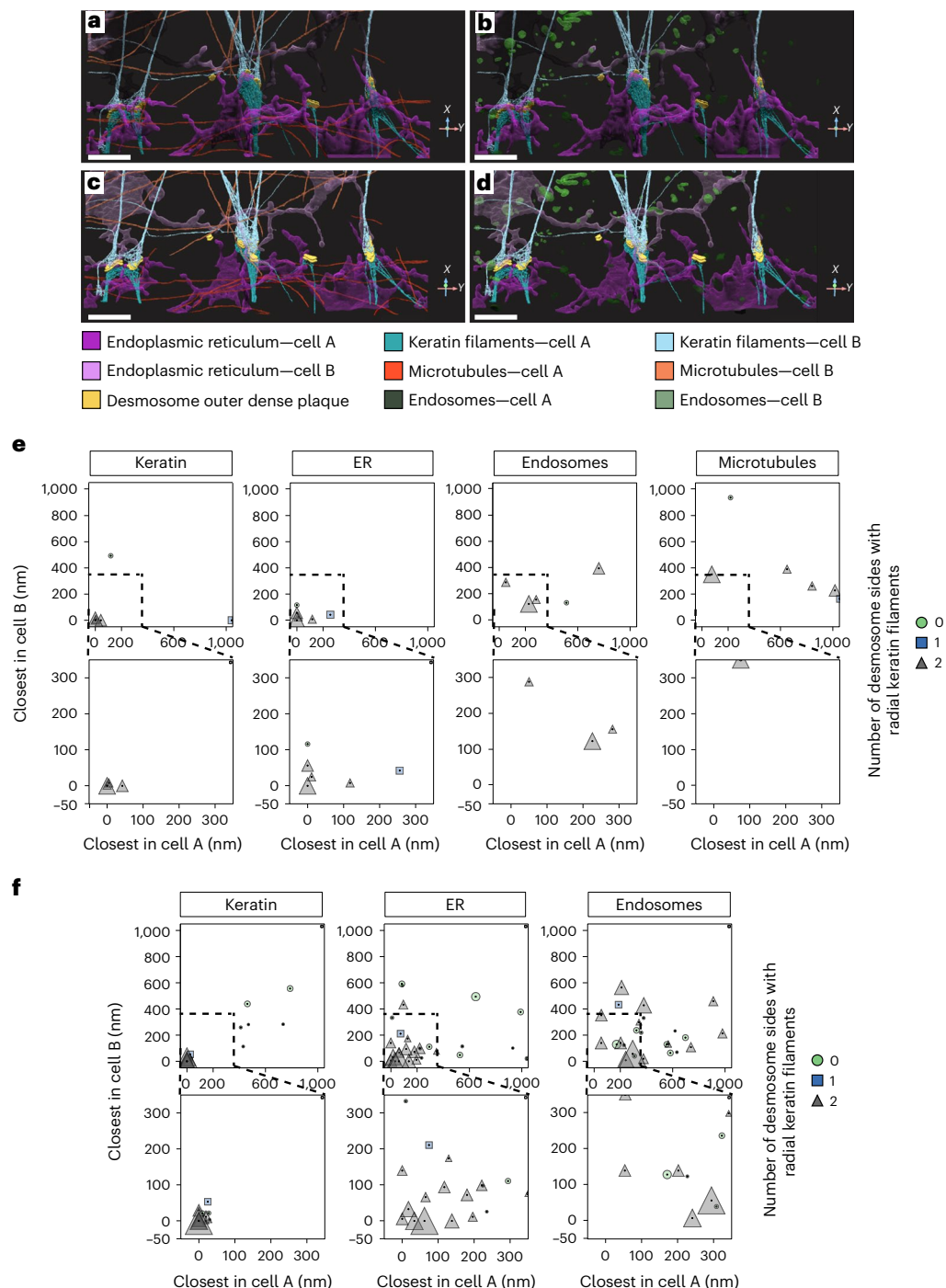
Fig. 3 | Analysis of FIB-SEM data reveals a symmetrical organization of ER and keratin filaments proximal to desmosomes. a–d, Rotated views of 3D reconstructions of the $4 \times 4 \times 4$ nm^3 dataset with either microtubules (orange) or endosomes (green) in addition to desmosomes (yellow), ER (magenta) and keratin (teal). Scale bar, 1 μm. **e**, Scatter plots representing the $4 \times 4 \times 4$ nm^3 dataset showing the distance from individual desmosomes to the closest organelles in each cell ($n = 6$ desmosomes at one cell–cell contact). **f**, Scatter plots representing the $8 \times 8 \times 8$ nm^3 dataset showing the distance from individual desmosomes to the closest organelles in each cell ($n = 27$ desmosomes at one cell–cell contact). The marker size is proportional to desmosome volume, with colour and shape showing whether a desmosome has radial keratin on both cytoplasmic faces (grey triangles), radial keratin on only one face (blue square), or no radial keratin on either face (green circles). Bottom row shows a magnification of the plots in the top row. Source numerical data are available in source data.

undergoing fusion (Extended Data Fig. 8a–f). Further analysis revealed that the tip of ER tubules always tracked with at least one of the DP puncta before fusion ($n = 67$ fusion events analysed) (Extended Data Fig. 8g–l) and remained associated with newly fused desmosomes (Extended Data Fig. 8g–l, bottom row). These ER–DP interactions persisted during successive fusion events (Supplementary Video 7). These findings

indicate that ER tubules associate with desmosomes under steady-state conditions and during desmosome remodelling events.

To determine the spatio-temporal behaviour of ER and desmosomes during de novo cell–cell contact formation, we grew cells in low calcium (~30 μM) culture conditions for 18–24 h to prevent desmosome formation. The calcium concentration was then raised
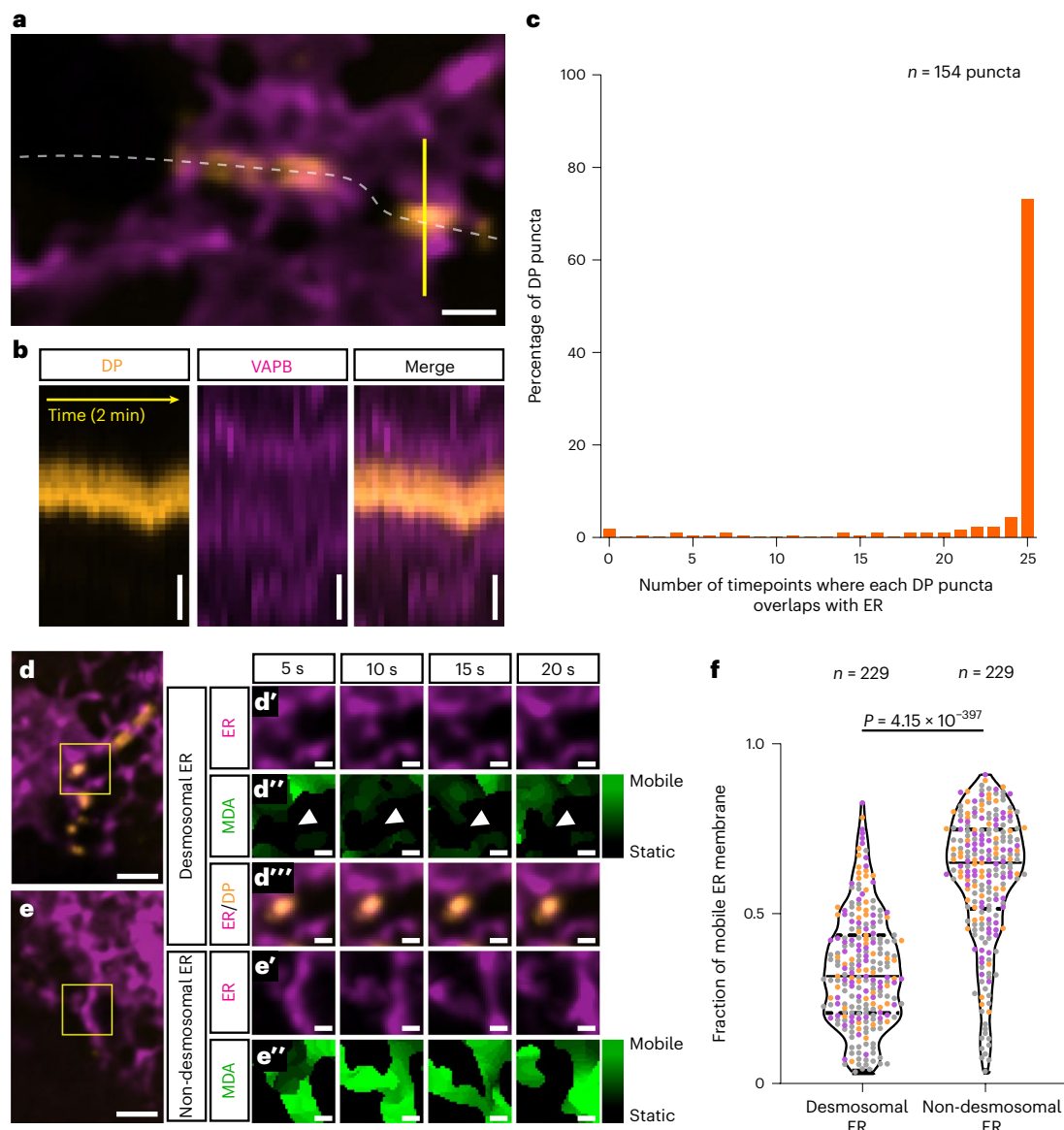
Fig. 4 | Desmosomes anchor ER tubules and stabilize ER membrane. a, Snapshot of a pair of A431 cells expressing DP-EGFP (orange, desmosome marker) and mApple-VAPB (magenta, ER marker) showing ER tubules anchored on either side of DP puncta. Dashed white line indicates cell–cell border. Solid yellow line indicates position of kymograph in **b** (images are representative of *n* = 34 fields from three independent experiments). Scale bar, 1 μm. **b,** Kymograph of yellow line in **a** revealing stable ER–DP co-localization over a 2 min time course. Scale bar, 500 nm. **c,** Histogram shows percentage of DP puncta that co-localize with ER for *t* timepoints over a 25 timepoint duration (*n* = 154 puncta in 34 fields from three independent experiments). **d,e,** Yellow boxes highlight representative regions analysed by MDA. Scale bar, 2 μm. **d′,d″,** ER (magenta), MDA-generated

ER movement (green), ER at desmosomes (orange). White arrowheads in **d′** depict location of DP puncta. **e′,e″,** ER (magenta), MDA-generated ER movement (green) at non-desmosomal regions. Bright green pixels in **d′** and **e′** depict ER fraction that is mobile between timepoints. Note more bright green pixels in **e′** versus **d′**, indicating more mobile ER. Scale bar, 500 nm. **f,** Violin plot depicting fraction of mobile ER in desmosomal (*n* = 229 ROIs in 34 fields) versus non-desmosomal (cytoplasmic) (*n* = 229 ROIs in 34 fields) regions. Exact *P* values are provided for each comparison (two-tailed Mann–Whitney test; *n* = 3 independent experiments). Horizontal solid black lines in violin plots represent medians and dashed lines represent first (lower) and third (upper) quartiles. Dots are colour-coded by replicate. Source numerical data are available in source data.

to physiological levels (1.8–2.7 mM) to initiate formation of cell–cell contact[16]. Immediately following the switch to normal calcium levels, we performed live-cell time-lapse imaging to track ER tubules as desmosome puncta form at cell–cell contacts. We observed that ER tubules extend towards the cell periphery a few minutes after cells initiate contact (Fig. 6a–e and Supplementary Fig. 2). When two adjacent cells came into contact, peripheral ER tubules formed mirror image-like structures at contacts and no longer retracted from the periphery (*n* = 12 pairs of contacting cells) (Fig. 6b and Supplementary Video 8). Additional examples are shown in Supplementary

Fig. 2 using fluorescently tagged wheat germ agglutinin (WGA) to highlight cell membranes. In all 12 instances where we visualized new cell–cell contact formation, nascent DP puncta became visible precisely where ER tubules had formed paired structures (Fig. 6c,d). As cell contacts matured, additional ER mirror image-like arrangements emerged and immobilized at sites of newly forming desmosome puncta (Fig. 6e).

We also monitored keratin filament and ER tubule dynamics following a calcium switch using A431 cells stably expressing fluorescently tagged keratin-14 (mNeonGreen-KRT14) and mApple-VAPB. Following
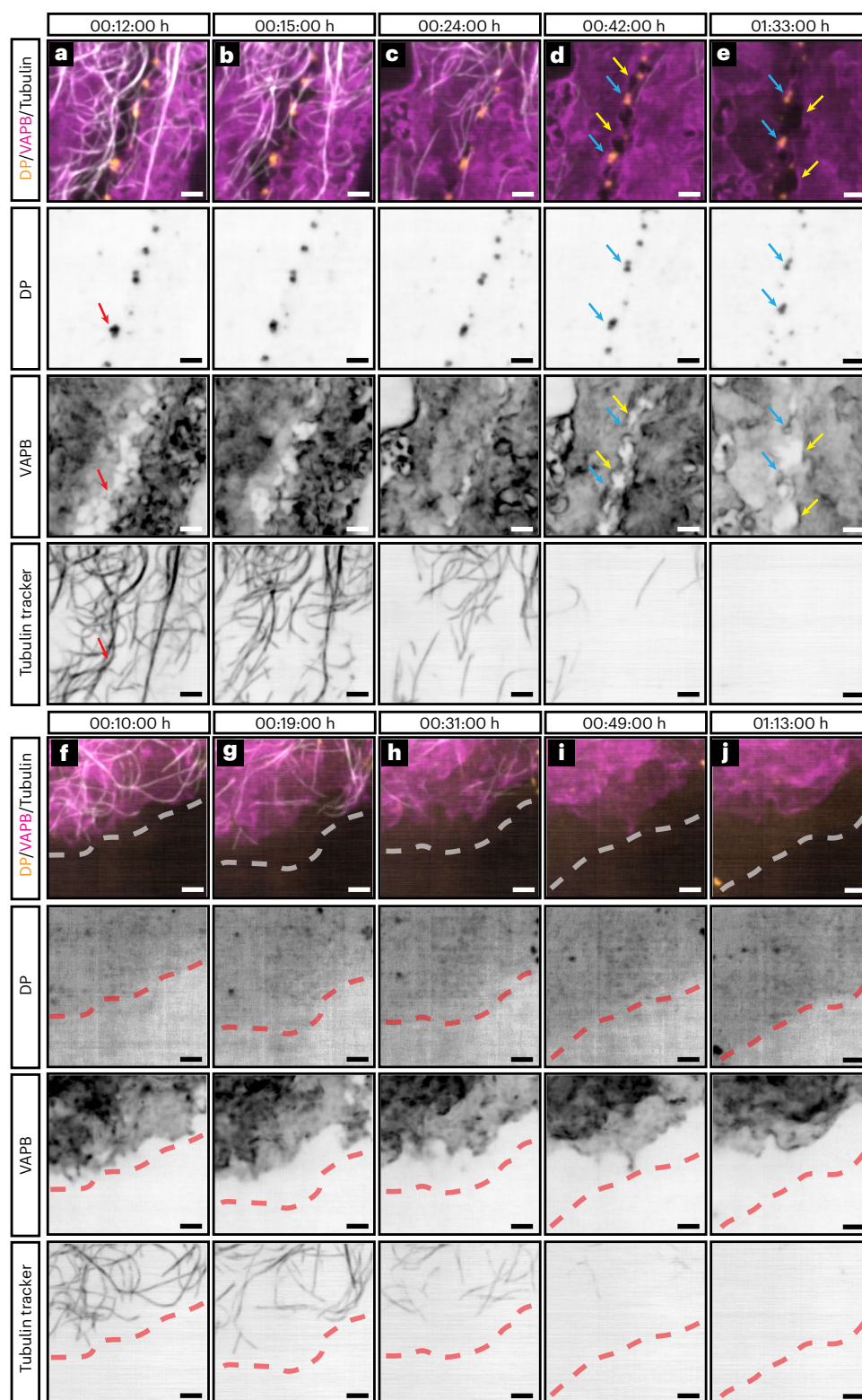
Fig. 5 | ER remains anchored to desmosomal junctions but retracts from cell-free edges when microtubules are depolymerized. a–e, Time course at cell–cell border of a pair of A431 cells expressing mApple-VAPB (ER marker, magenta) and DP-EGFP (desmosome marker, orange) treated with 30 μM nocodazole (images are representative of $n = 3$ independent experiments). Microtubules are labelled with TTDR (white). Microtubules are seen near desmosomes and ER tubules (red arrows) (**a**). As microtubules depolymerize, peripheral tubular ER becomes more sheet-like and remains tethered to desmosomes (**d** and **e**, blue arrows), but retracts from desmosome-free regions (**d** and **e**, yellow arrows). Scale bar, 2 μm. **f–j,** Time course at cell-free edge of an A431 cell expressing

mApple-VAPB and DP-EGFP treated with 30 μM nocodazole (images are representative of $n = 3$ independent experiments; some time lapses of cell-free edges are in the same FOV as time lapses of cell–cell borders). Peripheral ER is extended towards the cell-free edge when microtubules are present (**f**). As microtubules depolymerize, ER sheets retract from the cell-free edge (**h–j**). Timestamps indicate duration after addition of nocodazole. Cell-free edge is depicted by a dashed red or white line in **f–j**. Gamma correction was applied to some greyscale images. Gamma (inverted): 0.75 (**a–e**, VAPB channel) and 1.75 (**f–j**, DP channel). Scale bar, 2 μm.
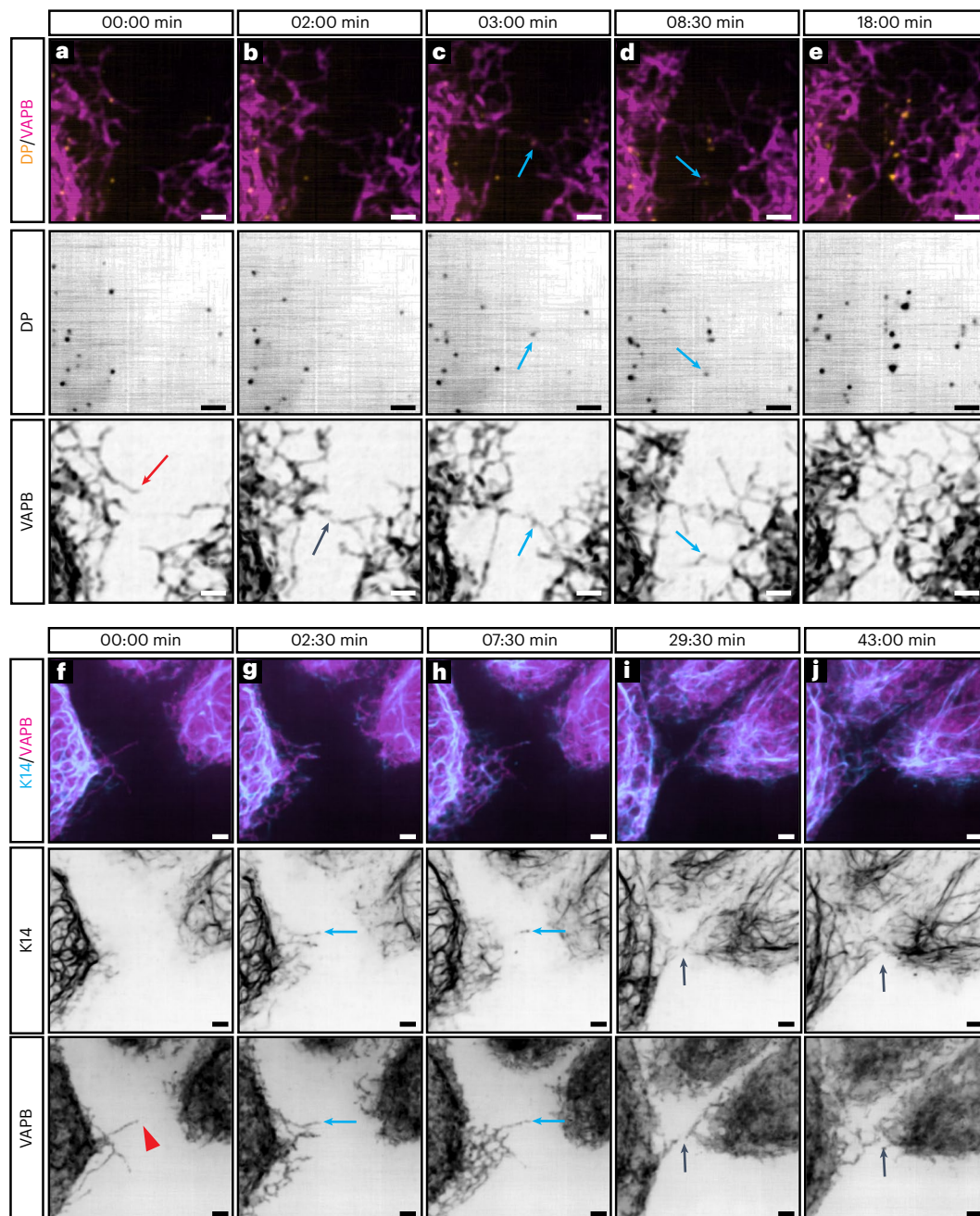
Fig. 6 | ER tubules associate with desmosomes and keratin filaments during assembly. a–e, Snapshots of a live-cell time-course of DP (orange) and VAPB (magenta) in A431 cells as they form cell–cell contacts (images are representative of $n = 12$ pairs of contacting cells from a total of three independent experiments). ER tubules first extend in both cells (**a**, red arrow), followed by formation of an ER mirror image at the cell–cell contact (**b**, black arrow). DP puncta appear at the exact position of an ER mirror image (**c** and **d**, blue arrows). Eventually, more DP puncta appear and ER mirror images form as contacts mature (**e**). Gamma correction was applied to greyscale images. Gamma (inverted): 1.25 (DP) and 1.5 (VAPB). Scale bar, 2 μm. **f–j,** Snapshots of a live-cell time course of keratin filaments (blue) and VAPB (magenta) in A431 cells as they form cell–cell contacts (images are representative of $n = 12$ pairs of contacting cells from a total of five independent experiments). ER tubules sometimes extend alone (**f**, red arrowhead). ER tubules and keratin filaments extend towards cell–cell contacts simultaneously over several minutes (**g** and **h**, blue arrows). Keratin filaments and ER tubules form mirror images as contacts mature (**i** and **j**, black arrows). Scale bar, 2 μm.

addition of calcium, peripheral ER tubules extend to and retract from the cell edge without any keratin filaments (Fig. 6f). Eventually, ER tubules and keratin filaments extended and retracted simultaneously ($n = 38/40$ cells initiating contact) and in close spatial proximity (Supplementary Video 9). These ER–keratin associations persisted for several minutes (Fig. 6g,h). As the cells come into contact, both ER tubules and keratin filaments form stable mirror image-like structures

on either side of the cell–cell contact (Fig. 6i,j). Collectively, these experiments indicate that DP puncta formation and keratin filament assembly are initiated at sites of ER tubule extensions at nascent epithelial cell–cell contacts.

A role for ER in desmosome assembly is suggested by autosomal dominant mutations in the ER-resident calcium pump, sarco/endoplasmic reticulum Ca^{2+}-ATPase 2 (SERCA2). Mutations in SERCA2 cause
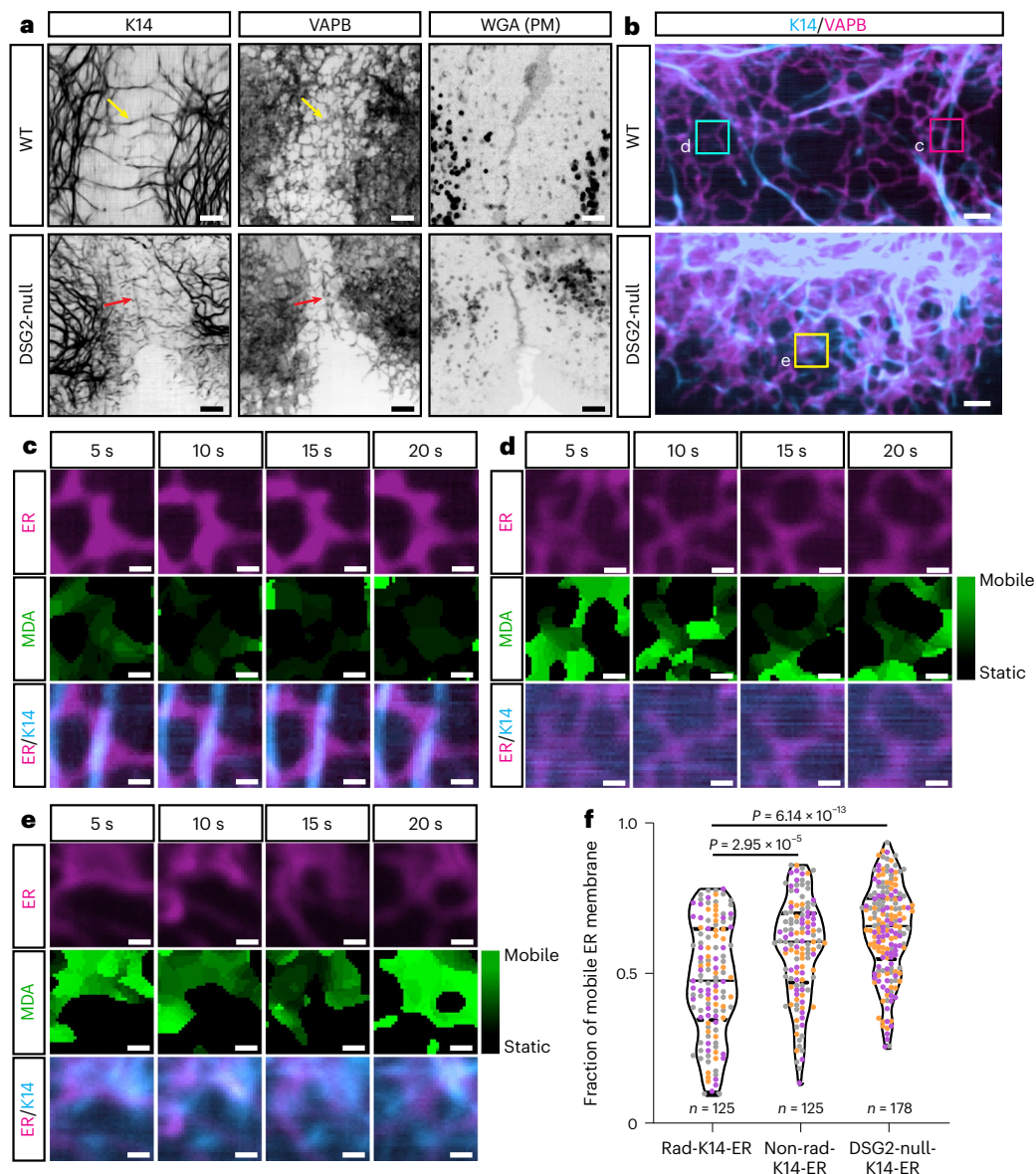
Fig. 7 | Desmosomes and keratin regulate peripheral ER organization and ER membrane stability. a, A431 WT cells (top row) or DSG-2 knockout cells (bottom row) expressing mNeonGreen-KRT14 (first column, keratin marker) and mApple-VAPB (middle column, ER marker) (images are representative of $n = 3$ independent experiments). WGA labels the PM. Yellow arrows show radial keratin filaments and associated VAPB tubules orthogonal to the PM in WT cells. Red arrows show keratin filaments and ER tubules parallel to the PM in DSG2-null cells. Gamma correction was applied to greyscale images. Gamma (inverted): 1.5 (KRT14 and VAPB channels). Scale bar, 4 µm. **b**, Representative light microscopy images of KRT14 (blue) and VAPB (magenta) in A431 WT and DSG2-null cells with regions analysed by MDA in **c** (pink box), **d** (blue box) and **e** (yellow box) (images are representative of $n = 3$ independent experiments). Scale bar, 2 µm. **c**, ER (magenta), MDA-generated ER movement (green) and ER at radial keratin

filaments (merge) in WT cells. **d**, ER (magenta), MDA-generated ER movement (green), ER at non-radial keratin filaments (merge) in WT cells. **e**, ER (magenta), MDA-generated ER movement (green) and ER at keratin filaments (merge) in DSG2-null cells. Bright-green pixels depict ER fraction that is mobile between timepoints. Scale bar, 500 nm (**c–e**). **f**, Violin plot depicting fraction of mobile ER along radial keratin in WT cells ($n = 125$ ROIs), non-radial keratin in WT cells ($n = 125$ ROIs in 25 fields) and keratin filaments in DSG2-null cells ($n = 178$ ROIs in 28 fields). Exact P values are provided for each comparison (two-tailed Mann–Whitney test; $n = 3$ independent experiments). Horizontal solid black lines in violin plots represent medians and dashed lines represent first (lower) and third (upper) quartiles. Dots are colour-coded by replicate. Source numerical data are available in source data.

Darier's disease, a skin disorder characterized by loss of desmosomal adhesion[17]. Inhibition of SERCA2 function with thapsigargin impairs DP localization to cell–cell borders in cultured cells[18]. Therefore, we used thapsigargin to determine if SERCA2 function is required for peripheral ER recruitment to nascent cell–cell contacts. We treated A431 cells expressing DP-EGFP and mApple-VAPB cultured in low-calcium medium with either DMSO or 1 µM thapsigargin for 30 min, followed by a switch to high-calcium (~2.7 mM) medium ($n = 3$ independent experiments). Similar to Fig. 6a–e, junctional DP puncta appeared following formation of ER tubule pairs at 100% ($n = 25/25$) of cell–cell borders of DMSO-treated cells (Extended Data Fig. 9a–e). However, in thapsigargin-treated cells, DP puncta appeared at only 44.8% ($n = 13/29$) of cell–cell borders. In those instances where no DP puncta appeared in thapsigargin-treated cells, ER tubules still extended towards the cell periphery (Extended Data Fig. 9f–j). These data indicate that ER tubule recruitment to nascent contacts precedes desmosome formation and

suggest that ER tubule regulation of local calcium levels is required for desmosome assembly to proceed.

Desmosomes and keratin regulate peripheral ER

To determine if desmosomes impact ER organization, we assessed ER and keratin distribution in wild-type (WT) A431 cells and in A431 cells in which the desmosomal cadherin desmoglein-2 (*DSG2*) gene was ablated using clustered regularly interspaced short palindromic repeats (CRISPR)/Cas9. These DSG2-null cells exhibit aberrant localization of desmosomal proteins and weakened cell–cell adhesion strength, while still forming adherens junctions[19]. We stably expressed mNeonGreen-KRT14 and mApple-VAPB in WT and DSG2-null cells and imaged these cells using spinning disk confocal microscopy. In WT cells, keratin filaments extended radially towards desmosomal junctions. These radial keratin filaments terminated at cell borders where they anchored to desmosomes (Fig. 7a; Supplementary Video 10, top row). Peripheral ER tubules exhibited similar organization in these cells, running parallel to the keratin filaments with both structures forming paired structures at cell–cell contacts (Fig. 7a, yellow arrows). In contrast, DSG2-null cells exhibited few radial keratin bundles. Instead, keratins in DSG2-null cells ran parallel to the PM in a subcortical localization (Fig. 7a and Supplementary Video 10, bottom row). Similarly, peripheral ER tubules were organized parallel to rather than orthogonally to cell–cell contacts (Fig. 7a, red arrows). These data indicate that loss of desmosomes alters peripheral ER organization.

We also assessed the influence of desmosomes on ER dynamics. MDA was used to determine ER membrane mobility at: (1) ER tubules along radial keratin filaments in WT cells, (2) ER tubules not associated with radial filaments in WT cells, and (3) ER tubules located along keratin filaments in DSG2-null cells (Fig. 7b–e). Analysis revealed that 52% of ER membrane was stable along radial keratin filaments running to desmosomes, whereas only 42% of ER associated with non-radial keratin filaments was stable. These differences were even more stark when assessing ER mobility in DSG2-null cells, with only 36% of keratin filament-associated ER membrane being stable (Fig. 7f). Together, these results indicate that an association between ER tubules and radial keratin filament bundles suppresses ER tubule dynamics. The stabilization of ER tubules along radial keratin filament bundles explains the persistence of ER tubule positioning in mirror image-like arrangements at desmosomal cell–cell junctions.

Keratin and desmosomes regulate ER morphology and ER stress

Keratin mutations result in a wide range of human diseases, often affecting the skin and skin appendages[20]. To determine if disease-causing mutations that disrupt keratin filaments also perturb ER morphology, we stably expressed a KRT14 point mutant, KRT14[R125C] (mNeonGreen-KRT14[R125C]), in A431 cells expressing mApple-VAPB. This KRT14 mutation results in the skin blistering disease epidermolysis bullosa simplex (EBS) by causing keratin filament aggregation[21]. Similar to results shown in Fig. 7, KRT14[WT] formed radial filaments closely associated with ER tubules (Fig. 8a–d and Supplementary Video 11, top row). In cells expressing the KRT14[R125C] mutant, peripheral ER morphology was sheet-like or planar, especially when in contact with keratin aggregates (Fig. 8e–h). Time-lapse microscopy revealed that ER stably associated with both filamentous and aggregated keratin (Extended Data Fig. 10a–h and Supplementary Video 11, bottom row). Quantification indicated that ~75–79% of the keratin aggregates maintain contact with ER membranes over a 2 min time course (Extended Data Fig. 10i). To verify that changes in ER morphology were not an artefact of differing levels of mApple-VAPB expression in different cells, we plated a mixture of KRT14[WT] and KRT14[R125C]-expressing A431 cells (1:1 ratio) onto slides and imaged mixed cell clusters that had similar fluorescence intensities of mApple-VAPB. Again, peripheral ER domains appeared more sheet-like in the KRT14[R125C]- expressing A431 cells (Fig. 8i–k and Supplementary Video 12). These results indicate that a

keratin mutation that causes an inherited epidermal blistering disease alters ER membrane morphology.

Transfection of HaCaT keratinocytes with the KRT14[R125C] mutant has been shown to upregulate ER stress markers phospho-c-Jun and BiP (*HSPA5*) (ref. 22). Therefore, we examined KRT14[WT]- or KRT14[R125C]-expressing A431 cells for changes in messenger RNA transcripts of multiple ER stress genes, including *DDIT3* (also known as CHOP), *XBP1s* (spliced isoform of XBP1), *ATF3* and *HSPA5* (also known as BiP or GRP78). A qRT–PCR analysis of RNA isolated from these cells revealed no significant differences in expression levels of *DDIT3*, *XBP1s* and *HSPA5*. However, there was a significant upregulation of *ATF3* in KRT14[R125C]-expressing cells (Fig. 8l). To determine if disruption of desmosomes also induces expression of ER stress transcripts, primary human keratinocytes were treated with autoantibodies (IgG) isolated from plasma of patients with pemphigus vulgaris (PV). In this disorder, patients generate function-blocking autoantibodies directed against the desmosomal cadherin desmoglein-3 (ref. 23). These autoantibodies cause desmosome disruption, keratin filament retraction and loss of adhesion strength[24,25]. Pemphigus patient IgG induced upregulation of *XBP1s*, *HSPA5* and *ATF3* expression compared with cells treated with normal human IgG (Fig. 8m). Together, these results indicate that perturbation of keratin organization or desmosome function is coupled to the upregulation of transcripts associated with ER stress responses.

Discussion

Our data reveal a previously unknown tripartite complex comprising desmosomes, keratin intermediate filaments and peripheral ER tubules. We report that desmosomes regulate peripheral ER morphology by organizing radial keratin filament bundles that position ER tubules orthogonally to the PMs of adjacent cells. These ER tubules exhibit frequent interactions with both keratin filament bundles and the substructure of the desmosome cytoplasmic plaque. This architectural arrangement, along with the characteristic mirror image organization of desmosomes, shapes the morphology and dynamic behaviour of peripheral ER membranes at regions of epithelial cell–cell contact.

The ER makes close (<30 nm) contacts with the PM that function as sites of lipid exchange and calcium homeostasis[1]. Epithelial cells assemble an extensive array of intercellular contacts that could influence or be regulated by ER–PM associations. A serial EM study of hepatocytes and epithelial spheroids found extensive ER–PM contacts at lateral PM domains, a few microns from tight junctions[21]. Another recent study suggested an association between ER and adherens junctions[26]. Further, the ER is associated with highly specialized complexes between Sertoli cells and developing spermatids where it is thought to regulate calcium signalling and junction remodelling[27]. We find that stable ER–desmosome associations occur at mature desmosomes, during desmosome fusion and during initial stages of desmosome formation. When cell–cell contact is initiated, ER tubules extend to the cell periphery and DP puncta appear to coalesce de novo at the tips of ER tubular extensions. Thus, the ER appears to pattern-specific PM regions for nascent desmosome formation, and reciprocally, newly forming desmosomes function as anchorage points that stabilize peripheral ER tubules. Additional studies will be needed to delineate the temporal hierarchy of ER recruitment to nascent cell–cell contacts in relation to other intercellular junctions and their associated cytoskeletal networks.

High-resolution FIB-SEM (resulting in 4 nm and 8 nm isotropic voxels) revealed that the ER membrane lies proximal to the desmosome plaque, often within distances observed at canonical ER–PM contacts (Figs. 1 and 2 and Supplementary Videos 1–3). In several instances, we observed ER tubules in physical contact with both the inner and outer dense plaque of the desmosome. In some desmosomes, tubules even penetrate the space between these electron-dense structures (Extended Data Fig. 3). These observations strongly suggest molecular associations between proteins resident on the ER membrane and within
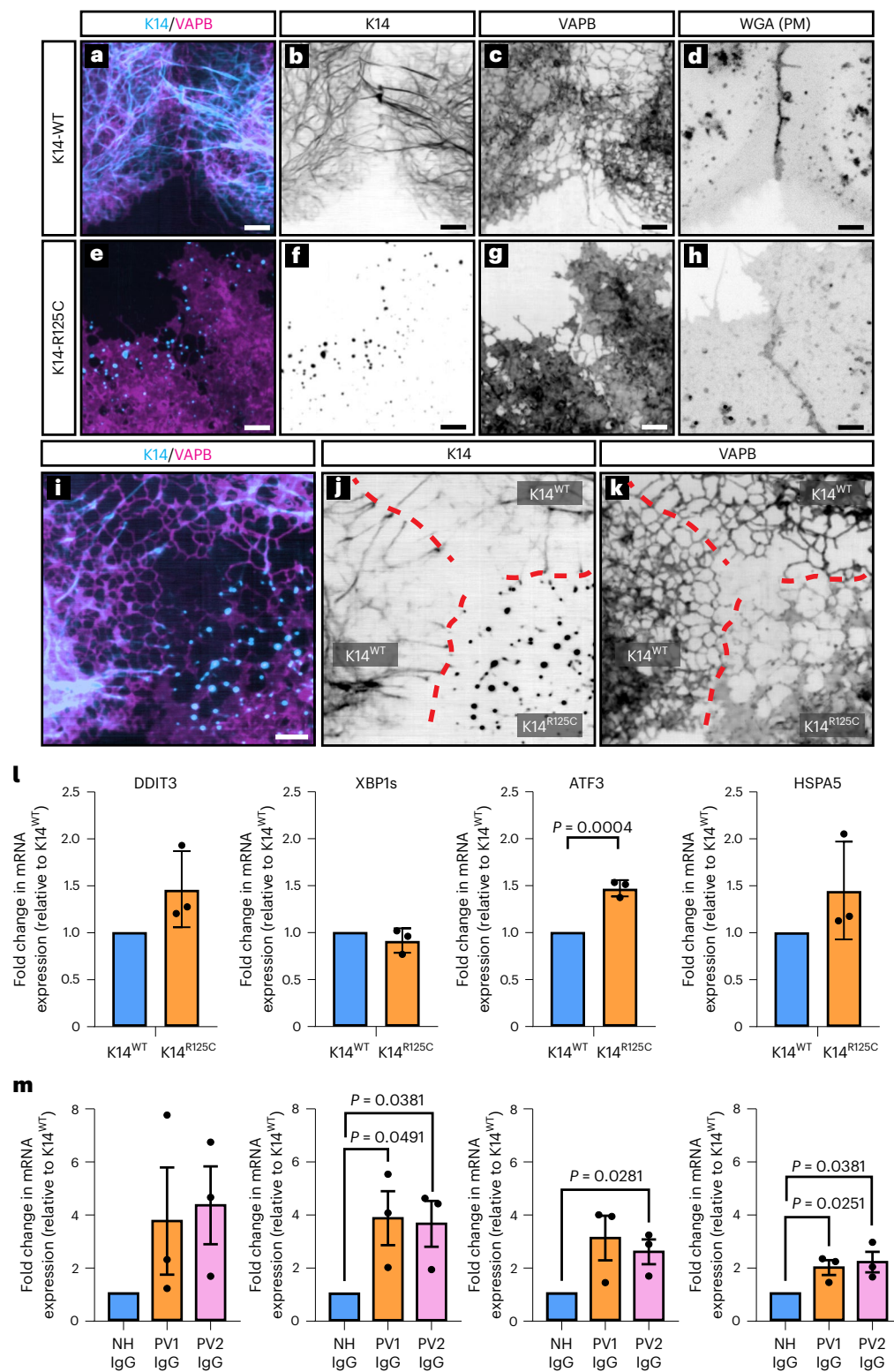
Fig. 8 | Keratin aggregation perturbs ER membrane morphology and alterations in keratin or desmosome function cause ER stress. a–d, Light microscopy of KRT14^{WT}, VAPB and PM in A431 cells showing ER with tubular morphology (images are representative of $n = 3$ independent experiments). Scale bar, 4 μm. **e–h**, A431 expressing KRT14^{R125C} aggregates showing ER with sheet-like morphology. PM is labelled with WGA conjugated with a fluorescent dye (images are representative of $n = 3$ independent experiments). Scale bar, 4 μm. **i–k**, A431 cells expressing KRT14^{WT} (top and left cells) or KRT14^{R125C} (bottom right cell) showing tubular ER in KRT14^{WT}-expressing cells and sheet-like ER membrane in KRT14^{R125C}-expressing cells (images are representative of $n = 3$ independent experiments). Red dashed lines indicate PM. Gamma correction was applied to greyscale images. Gamma (inverted): 1.5 (**b**, **c**, **f**, **g** and **k**). Scale bar, 4 μm. **l**, Fold change in mRNA expression levels of *DDIT3*, *XBP1s*, *ATF3* and *HSPA5* between A431 cells expressing KRT14^{WT} or KRT14^{R125C}. Data are presented as mean ± s.e.m. Exact P values are provided for each comparison when statistically significant (two-tailed *t*-test; $n = 3$ independent experiments). **m**, Fold change in mRNA expression levels of *DDIT3*, *XBP1s*, *ATF3* and *HSPA5* between primary human keratinocytes treated with either normal human IgG or IgG isolated from two different patients with PV to disrupt desmosomal adhesion. Data are presented as mean ± s.e.m. Exact P values are provided for each comparison when statistically significant (two-tailed *t*-test; $n = 3$ independent experiments). Source numerical data are available in source data.

the desmosomal substructure. This notion is supported further by optical imaging of living cells. ER tubules associated with desmosomes exhibit reduced mobility compared with non-desmosomal ER (Fig. 4). Knockout of the desmosomal cadherin DSG2 reduced desmosome formation and increased peripheral ER membrane mobility (Fig. 7). These observations indicate that desmosomes control both the organization and dynamics of peripheral ER membranes.

Three-dimensional reconstructions of FIB-SEM datasets also revealed interactions between ER tubules and keratin filaments running orthogonally towards desmosomal junctions (Fig. 2). ER membrane frequently surrounded keratin filament bundles (Fig. 2a,b). Consequently, ER tubules and keratin filaments displayed a coordinated spatial and temporal relationship in live cell systems. During cell–cell contact formation, keratin filaments extend along ER tubular extensions, resulting in a stabilized mirror image-like arrangement of tubules and keratin filaments terminating at sites of desmosome maturation (Figs. 6f–j and 7). Desmoglein-null cells exhibit a loss of keratin bundles extending out to the cell periphery and a loss of orthogonally organized ER at cell–cell contacts (Fig. 7). Likewise, keratin filament aggregation caused a dramatic re-organization of ER membranes (Fig. 8). In cells expressing WT KRT14, peripheral ER was predominantly tubular. In contrast, expression of an EBS-causing K14 mutant that results in keratin aggregation reduced tubular ER in favour of planar ER membrane morphology. These findings indicate that desmosomes function to anchor keratin filament bundles that in turn act as filamentous guides that stabilize ER tubules into mirror image-like arrangements at epithelial cell–cell junctions. Disruption of either desmosomal or keratin organization profoundly impacts both ER dynamics and morphology.

The identification of an ER–desmosome complex provides a foundation for new ways to conceive of cellular stress signalling mechanisms. Cell stress signalling is a central function of the ER[28], and intermediate filaments provide cells and tissues with resistance to mechanical and chemical stresses[20,29,30]. Keratin filaments interact with the nuclear envelope, an extension of the ER, and keratin 14 loss alters nuclear shape, further suggesting a link between ER–keratin associations and cell signalling[31,32]. ER stress has been implicated in epidermal fragility disorders caused by keratin mutations[33]. Similarly, ER stress transcripts are increased when keratin or desmosome organization is perturbed (Fig. 8l,m). Conversely, loss-of-function mutations in the ER calcium pump SERCA2 cause desmosome defects in Darier's disease, and pharmacological inhibition of SERCA2 in vitro prevents desmosome assembly[18,34] (Extended Data Fig. 9). SERCA2 and the ER shaping protein reticulon-4 have recently been identified as putative DP binding partners[35], suggesting direct links between ER regulatory proteins and desmosome structural elements. These observations suggest that the ER–desmosome architecture reported here regulates desmosome assembly at nascent cell–cell contacts and mediates cellular stress signalling when desmosome or intermediate filament structure is compromised.

Online content

Any methods, additional references, Nature Portfolio reporting summaries, source data, extended data, supplementary information, acknowledgements, peer review information; details of author contributions and competing interests; and statements of data and code availability are available at https://doi.org/10.1038/s41556-023-01154-4.

References

1. Wu, H., Carvalho, P. & Voeltz, G. K. Here, there, and everywhere: the importance of ER membrane contact sites. *Science* **361**, eaan5835 (2018).
2. Schwarz, D. S. & Blower, M. D. The endoplasmic reticulum: structure, function and response to cellular signaling. *Cell. Mol. Life Sci.* **73**, 79–94 (2016).
3. Prinz, W. A., Toulmay, A. & Balla, T. The functional universe of membrane contact sites. *Nat. Rev. Mol. Cell Biol.* **21**, 7–24 (2020).
4. Cohen, S., Valm, A. M. & Lippincott-Schwartz, J. Interacting organelles. *Curr. Opin. Cell Biol.* **53**, 84–91 (2018).
5. Perkins, H. T. & Allan, V. Intertwined and finely balanced: endoplasmic reticulum morphology, dynamics, function, and diseases. *Cells* **10**, 2341 (2021).
6. Hoffman, D. P. et al. Correlative three-dimensional super-resolution and block-face electron microscopy of whole vitreously frozen cells. *Science* **367**, eaaz5357 (2020).
7. Godsel, L. M. et al. Desmoplakin assembly dynamics in four dimensions. *J. Cell Biol.* **171**, 1045–1059 (2005).
8. Zewe, J. P., Wills, R. C., Sangappa, S., Goulden, B. D. & Hammond, G. R. SAC1 degrades its lipid substrate PtdIns4P in the endoplasmic reticulum to maintain a steep chemical gradient with donor membranes. *eLife* **7**, e35588 (2018).
9. Johnson, B. et al. Kv2 potassium channels form endoplasmic reticulum/plasma membrane junctions via interaction with VAPA and VAPB. *Proc. Natl Acad. Sci. USA* **115**, E7331–E7340 (2018).
10. Stahley, S. N., Bartle, E. I., Atkinson, C. E., Kowalczyk, A. P. & Mattheyses, A. L. Molecular organization of the desmosome as revealed by direct stochastic optical reconstruction microscopy. *J. Cell Sci.* **129**, 2897–2904 (2016).
11. North, A. J. et al. Molecular map of the desmosomal plaque. *J. Cell Sci.* **112**, 4325–4336 (1999).
12. Waterman-Storer, C. M. & Salmon, E. D. Endoplasmic reticulum membrane tubules are distributed by microtubules in living cells using three distinct mechanisms. *Curr. Biol.* **8**, 798–807 (1998).
13. Terasaki, M., Chen, L. B. & Fujiwara, K. Microtubules and the endoplasmic reticulum are highly interdependent structures. *J. Cell Biol.* **103**, 1557–1568 (1986).
14. Spits, M. et al. Mobile late endosomes modulate peripheral endoplasmic reticulum network architecture. *EMBO Rep.* **22**, e50815 (2021).
15. Gloushankova, N. A., Wakatsuki, T., Troyanovsky, R. B., Elson, E. & Troyanovsky, S. M. Continual assembly of desmosomes within stable intercellular contacts of epithelial A-431 cells. *Cell Tissue Res.* **314**, 399–410 (2003).
16. Hennings, H. & Holbrook, K. A. Calcium regulation of cell–cell contact and differentiation of epidermal cells in culture. An ultrastructural study. *Exp. Cell. Res.* **143**, 127–142 (1983).
17. Cooper, S. M. & Burge, S. M. Darier's disease: epidemiology, pathophysiology, and management. *Am. J. Clin. Dermatol.* **4**, 97–105 (2003).
18. Hobbs, R. P. et al. The calcium ATPase SERCA2 regulates desmoplakin dynamics and intercellular adhesive strength through modulation of PKCα signaling. *FASEB J.* **25**, 990–1001 (2011).
19. Zimmer, S. E. et al. Differential pathomechanisms of desmoglein 1 transmembrane domain mutations in skin disease. *J. Invest. Dermatol.* **142**, 323–332.e8 (2022).
20. Jacob, J. T., Coulombe, P. A., Kwan, R. & Omary, M. B. Types I and II keratin intermediate filaments. *Cold Spring Harb. Perspect. Biol.* **10**, a018275 (2018).
21. Chung, G. H. C. et al. The ultrastructural organization of endoplasmic reticulum–plasma membrane contacts is conserved in epithelial cells. *Mol. Biol. Cell.* **33**, ar113 (2022).
22. Yoneda, K. et al. An autocrine/paracrine loop linking keratin 14 aggregates to tumor necrosis factor α-mediated cytotoxicity in a keratinocyte model of epidermolysis bullosa simplex. *J. Biol. Chem.* **279**, 7296–7303 (2004).
23. Amagai, M. & Stanley, J. R. Desmoglein as a target in skin disease and beyond. *J. Invest. Dermatol.* **132**, 776–784 (2012).
24. Stahley, S. N. & Kowalczyk, A. P. Desmosomes in acquired disease. *Cell Tissue Res.* **360**, 439–456 (2015).

25. Ellebrecht, C. T., Maseda, D. & Payne, A. S. Pemphigus and pemphigoid: from disease mechanisms to druggable pathways. *J. Invest. Dermatol.* **142**, 907–914 (2022).

26. Joy-Immediato, M. et al. Junctional ER organization affects mechanotransduction at cadherin-mediated adhesions. *Front. Cell Dev. Biol.* **9**, 669086 (2021).

27. Vogl, A. W., Lyon, K., Adams, A., Piva, M. & Nassour, V. The endoplasmic reticulum, calcium signaling and junction turnover in Sertoli cells. *Reproduction* **5**, R93–R104 (2018).

28. Hetz, C., Zhang, K. & Kaufman, R. J. Mechanisms, regulation and functions of the unfolded protein response. *Nat. Rev. Mol. Cell Biol.* **21**, 421–438 (2020).

29. van Bodegraven, E. J. & Etienne-Manneville, S. Intermediate filaments from tissue integrity to single molecule mechanics. *Cells* **10**, 1905 (2021).

30. Redmond, C. J. & Coulombe, P. A. Intermediate filaments as effectors of differentiation. *Curr. Opin. Cell Biol.* **68**, 155–162 (2021).

31. Lee, C. H., Kim, M. S., Chung, B. M., Leahy, D. J. & Coulombe, P. A. Structural basis for heteromeric assembly and perinuclear organization of keratin filaments. *Nat. Struct. Mol. Biol.* **19**, 707–715 (2012).

32. Jorgens, D. M. et al. Deep nuclear invaginations are linked to cytoskeletal filaments—integrated bioimaging of epithelial cells in 3D culture. *J. Cell Sci.* **130**, 177–189 (2017).

33. Evtushenko, N. A., Beilin, A. K., Kosykh, A. V., Vorotelyak, E. A. & Gurskaya, N. G. Keratins as an inflammation trigger point in epidermolysis bullosa simplex. *Int. J. Mol. Sci.* **22**, 12446 (2021).

34. Savignac, M., Simon, M., Edir, A., Guibbal, L. & Hovnanian, A. SERCA2 dysfunction in darier disease causes endoplasmic reticulum stress and impaired cell-to-cell adhesion strength: rescue by miglustat. *J. Invest. Dermatol.* **134**, 1961–1970 (2014).

35. Badu-Nkansah, K. A. & Lechler, T. Proteomic analysis of desmosomes reveals novel components required for epidermal integrity. *Mol. Biol. Cell.* **31**, 1140–1153 (2020).

COSEM Project Team

Stephan Preibisch[2], Eric T. Trautman[2], Larissa Heinrich[2], John Bogovic[2], Davis Bennett[2], David Ackerman[2], Woohyun Park[2], Alyson Petruncio[2], Stephan Saalfeld[2] & Aubrey V. Weigel[2]

Methods

Approvals

Gut and skin samples were excised from Sprague Dawley rats according to protocols approved by Animal Care Committees at the respective institutions: Animal care protocol AUP 21-02-01 to Charlis Raineki, Brock University; Animal care protocol A20-0076 to A.W.V., University of British Columbia, Canada. Some experiments described in this manuscript involved the use of discarded and/or de-identified human skin and pemphigus patient sera. These experiments were reviewed and determined to be 'not human subjects research' by the institutional review board at the Pennsylvania State University Office for Research Protections (PSU IRB STUDY00021792).

Lentivirus generation

To generate a lentiviral construct expressing mApple-VAPB, the VAPB open reading frame from mCherry-VAPB[8] was cloned into the C-terminus of mApple-C1 (ref. [36]) using in vivo assembly[37]. This step generates mApple-VAPB with a 15 bp linker (5'-TCCGGACTCAGATCT-3') between the mApple and VAPB open reading frames. A second round of in vivo assembly was performed to clone mApple-VAPB into the vector backbone of pLenti6-V5-DEST for lentivirus production. The remaining lentiviruses used in this study were generated by VectorBuilder. Vector IDs are specified in Supplementary Table 1 and can be used to retrieve detailed information about the vector on vectorbuilder.com. The sequences of plasmids we generated in-house were confirmed by sequencing and with restriction enzyme digestion. The sequences of all plasmids obtained from VectorBuilder were validated with restriction enzyme digestion. Lentiviruses were made by co-transfection into human embryonic kidney-293FT cells with pMD2.G (encoding VSV-G) and psPAX2 (encoding Gag and Pol) and collection of culture supernatants 24–72 h after transfection. Lentivirus was concentrated either by high-speed centrifugation at 4 °C for 1.5 h at -100,000g, or with the Lenti-X Concentrator kit (631231; Takara Bio) following the manufacturer's protocol. The mCherry-VAPB (gift from Gerry Hammond, plasmid #108126), mApple-C1 (gift from Michael Davidson, plasmid #54631), pMD2.G and psPAX2 (gifts from Didier Trono, plasmid #12259 and #12260, respectively) plasmids were obtained from Addgene. Plasmid sequences are available at ref. [38].

Cell line generation, transfection, culture and reagents

A431 epithelial cells and HaCaT keratinocytes were cultured in Dulbecco's modified Eagle medium (10-013-CV; Corning) with 10% foetal bovine serum (TET tested, S10350; R&D Systems) and 1× antibiotic–antimycotic solution (30-004-CI; Corning).

Primary NHEKs were isolated from neonatal foreskin as previously described[39,40]. NHEKs were cultured in KGM Gold Keratinocyte Growth Medium BulletKit (00192060; Lonza). For daily maintenance and subculturing of NHEKs, the final calcium concentration was adjusted to 50 µM to prevent desmosome formation.

CRISPR/Cas9 was used to knock out DSG2 (DSG2 gRNA target sequence GTTACGCTTTGGATGCAAG) in A431 cells[19,41]. DP-EGFP expression in A431 cells stably expressing Tet-On DP-EGFP was induced by culturing the cell lines in 4 µg ml⁻¹ doxycycline (D3447; Sigma-Aldrich) for 18–24 h (ref. [7]). A431 cells were transduced with lentivirus by incubating cells with 8–10 µg ml⁻¹ polybrene (TR-1003-G; EMD Millipore) in cell culture medium for 24–48 h. Cells stably infected with lentiviruses were selected using either blasticidin (2.5–5 µg ml⁻¹) (R21001; Thermo Fisher Scientific) or puromycin (0.5 µg ml⁻¹) (ABT-440; Boston BioProducts) or a combination of both, depending on the lentivirus used. Bulk sorting of cell lines expressing the various constructs was performed by fluorescence-activated cell sorting to obtain populations with similar expression levels.

Cells were also transiently transfected with mCherry-VAPB and DP-EGFP plasmids (Extended Data Fig. 1a,b) using the Viromer RED transfection reagent (TT100302; OriGene Technologies). Briefly, cells

were grown to 50% confluency. A mix of the Viromer RED transfection reagent, Viromer RED buffer and plasmid DNA were added to the cells and incubated. Cells were then imaged 24 h later. The DP-GFP (gift from Kathleen Green, plasmid #32227) was obtained from Addgene.

Antibodies

The following antibodies were used for western blot: 1:1,000 rabbit anti-DP (A303-356A; Bethyl Laboratories), 1:1,000 rabbit anti-VAPB (PA5-53023; Invitrogen) and 1:60,000 rabbit anti-GAPDH (10494-1-AP; Proteintech). Secondary antibodies used were: 1:3,000 goat anti-rabbit IgG (H + L) horseradish peroxidase conjugate (170-6515; Bio-Rad).

Western blotting

Cells were grown to 90% confluence in six-well plates and then incubated with either DMSO or 4 µg ml⁻¹ doxycycline 24 h before collection. When at 100% confluence, cells were rinsed 2× with cold 1× PBS+. Cells were then incubated in 2× Laemmli buffer (1610737; Bio-Rad) with β-mercaptoethanol (M2650; Sigma-Aldrich) for 1 min. on ice. Lysates were then scraped with a cell scraper and homogenized using a syringe and 25 G 5/8 needle. Cell lysates were then incubated at 95 °C for 5 min. Proteins were then separated on a 7.5% Mini-PROTEAN TGX gel (4561025; Bio-Rad) along with a protein ladder (PI26634; Thermo Scientific) using Tris/glycine/SDS running buffer (161−0732; Bio-Rad) and run at 10 mA for 7 min, then 30 mA for 7 min, then 80 mA for 10–15 min. Gels were then carefully transferred to 2× transfer buffer (161−0734; Bio-Rad) containing 20% methanol. Transfer to a nitrocellulose membrane (88018; Thermo Fisher Scientific) was performed overnight at 10 V. Blocking was performed with 5% milk (in 1× PBS-Tween) for 1 h. Membranes were incubated with primary antibodies (in 1× PBS-Tween) at 4 °C overnight. Membranes were washed three to six times with 1× PBS-Tween, followed by incubation in secondary antibody for 1 h, followed by three to six washes again. When necessary, membranes were stripped with OneMinute Stripping Buffer (GM6001; GM Biosciences), followed by a 1 h block. The above wash and incubation steps were then repeated for the next primary and secondary antibodies. Western blots were developed with chemiluminescence horseradish peroxidase substrate (RPN2106; GE Healthcare). The chemiluminescent blots were imaged with a ChemiDoc MP Imaging System (Bio-Rad). Densitometric analysis was performed using Fiji/ImageJ (v1.53t).

Levels of mApple-VAPB were quantified from lysates of DP-EGFP/mApple-VAPB A431 cells treated with either DMSO or 4 µg ml⁻¹ doxycycline and were found to be ~1.2–1.5× that of endogenous VAPB (Supplementary Fig. 3).

WGA labelling

Cells were incubated with 2–4 µg ml⁻¹ WGA (29026; Biotium) in 1× HBSS+ (Hank's Balanced Salt Solution) or 1× HBSS− (for calcium switch experiments) at 37 °C for 15 min. Cells were then washed once with 1× HBSS+ or 1× HBSS− (for calcium switch experiments). Pre-warmed live-cell imaging media was added to the cells before imaging.

TTDR labelling and nocodazole treatment

Cells were incubated with a 1:1,000 dilution of TTDR (T34076; Invitrogen) in 1× HBSS+ at 37 °C for 30 min. Cells were then washed once with 1× HBSS+. Pre-warmed live-cell imaging medium containing 30 µM nocodazole (in DMSO) (M-1404; Sigma) or an equivalent amount of DMSO only was added to the cells immediately before imaging.

DSG3 labelling in NHEKs

NHEKs were seeded on 35 mm #1.5 glass-bottom dishes with four compartments (#627870; Greiner Bio-One). Cells were switched to medium containing 550 µM calcium chloride for 18–24 h before labelling. To label DSG3, we used an Alexa Fluor 488-conjugated pathogenic mouse monoclonal antibody against the extracellular domain of Dsg3, AK23 (ref. [42]). Cells were incubated with 1:300 AF488-AK23 in ice-cold KGM

Gold Keratinocyte Growth Medium at 4 °C for 45 min. Cells were then washed three times with 1× HBSS. After the last wash, pre-warmed medium was added to the cells before imaging.

Treatment of cells with PV IgG

Desmosome formation in NHEK (no later than passage 3) was first induced by switching to culture medium containing 550 μM calcium for 16–18 h. Cells were treated with either normal human IgG or PV IgG at a final concentration of 400 μg ml^{-1} for 24 h at 37 °C. PV sera were kind gifts from Dr Masayuki Amagai (Keio University, Tokyo). PV sera used in this study were IgG preparations from two patients and predominately recognized Dsg3 (ELISA scores: PV1 - Dsg3 179.3, Dsg1 2.6; PV2 - Dsg3, 167.7; Dsg1, 4.1) (refs. [43],[44]).

Transmission EM

Cells cultured to 100% confluence on 12 mm, 0.4 μm, polyester transwells (CLS3460; Corning) were fixed in 1.5% paraformaldehyde (15713; Electron Microscopy Sciences (EMS)/1.5% glutaraldehyde (16320; EMS) in 0.1 M sodium cacodylate buffer (pH 7.3) (12300; EMS) at room temperature for 30 min. Rat skin and colon tissue from Sprague Dawley rats were also fixed as above. The membrane inserts were then cut out with a clean scalpel and incubated in room-temperature fixative. Membranes were then washed three times with 0.1 M sodium cacodylate buffer for 10 min each. Samples were then post-fixed on ice for 1 h with 1% OsO$_4$ (19100; EMS) (1:1 mix of 2% OsO$_4$ and 0.2 M sodium cacodylate buffer) and then washed three times (10 min each) with ddH$_2$O. Membranes were stained with 1% aqueous uranyl acetate and washed again three times (10 min each) with ddH$_2$O before being dehydrated in an ascending concentration series of ethanol solutions, treated with two changes of 100% propylene oxide (20401; EMS), and infiltrated with a 1:1 mix of propylene oxide and EMbed 812 resin (14120; EMS) and left overnight. After two 2 h incubations in 100% EMbed 812 resin, the membranes were placed on a silicone platform with cells facing up and embedding capsules (filled with resin) were inverted onto the membranes. Finally, the samples were heated in a 60 °C oven for 48 h. Polymerized blocks with membranes attached were removed from the silicone platforms and trimmed. Thin sections were cut on a Leica Ultramicrotome, and the sections collected on 200 mesh copper grids (G200-Cu; EMS). The sections were stained with uranyl acetate and lead citrate, and imaged on an FEI Tecnai G2 or Talos transmission electron microscope operated at 120 kV.

CLEM

Correlative light and electron microscopy (CLEM) was performed according to Hoffman et al.[6] and as described below.

Sapphire disk preparation. Optically flat sapphire disks (3 mm diameter, 50–80 μm thick; Nanjing Co-Energy Optical Crystal) were cleaned using basic Piranha solution (5:1:1 mixture of H$_2$O:50% H$_2$O$_2$:NH$_3$OH) for 4–6 h at 80–90 °C. Disks were then coated (Desk II sputter coater; Denton Vacuum) with a gold pattern around the outer 0.5 mm edge to identify the direction the disk is facing. Disks were then placed in a 20 mm MatTek disk, gold side facing down, submerged in 70% ethanol for 2–3 min. Ethanol was discarded, and disks were rinsed three times in sterile water and left to dry. Disks were then coated with 0.1% gelatin in 1:1 H$_2$O:growth medium for 1 h at 37 °C and left to dry.

Cell culture and staining for CLEM. Cultured A431 cells stably expressing DP-EGFP and mApple-VAPB at 70–80% confluency (maintained at 37 °C/5% CO$_2$ in 100 mm tissue culture dishes) were trypsinized (0.25% trypsin–EDTA) at 37 °C, resuspended and re-cultured onto the non-gold bearing surface of the sapphire disks. After 24 h, cells were incubated in 4 μg ml^{-1} doxycycline for DP-EGFP induction. After 24–48 h, cells were stained with MitoTracker Deep Red (M22426; Molecular Probes; working concentration 25–500 nM) at 50 nM or MitoView 650 (70075;

Biotium; working concentration 25–500 nM) in a CO$_2$ incubator for 15 min and washed.

High-pressure freezing. Sapphire disks containing labelled cells were dipped three times in freezing medium containing Fluorobrite medium (A1896702; Thermo Fisher), 25% dextran (Mr ~40,000, 31389-100G; Sigma), and 0.8 pM TetraSpeck microspheres (0.2 μm diameter, T7280; Invitrogen). They were then placed between aluminium planchettes and subjected to high-pressure freezing (HPF Compact 01; Wohlwend GmbH) according to the manufacturer's instructions. Samples were then stored in liquid N$_2$.

Optical imaging/Cryo-SIM. Specimen fluorescence was imaged using the setup described previously[6]. Briefly, residual ice on the non-cell bearing side of the sapphire disks was removed via scalpel scraping under liquid N$_2$. Samples were then loaded into a custom-built cryostat with an imaging window that maintained sample temperature of -77 K for the duration of imaging. Cells were excited via 488 nm (4 W, Genesis CX STM; Coherent), 561 nm (5 W, 2RU-VFLP-5000-560-B1R; MPB Communications) and 642 nm laser (2 W, 2RU-VFL-P-2000-642-B1R; MPB Communications) illumination and imaged via a 100×, 0.85 numerical aperture (NA) objective lens (CFI L Plan EPI CRB; Nikon) onto an sCMOS camera detector (Orca Flash 4.0 v3; Hamamatsu Corp.).

After correction-collar optimization (using TetraSpeck beads), montage epifluorescence images were taken of each coverslip to identify ROIs. Following this, ROIs were imaged using 3D structured illumination microscopy, with typical field of view (FOV) of 130 × 130 μm (*xy*) and 8 μm (*z*-depth). Images were processed using the SIM reconstruction algorithm reported previously[45], with the following typical reconstruction parameters: 0.007 Wiener Filter, 0.7 gamma apodization, 15-pixel radii of the singularity suppression at the optical transfer function origins. Finally, chromatic shifts between each colour channel were digitally corrected using the TetraSpeck beads as alignment fiducials.

EM preparation. Samples were unloaded from the cryo-fluorescence microscope and again stored in liquid N$_2$. They were then transferred to cryotubes containing 1–2% OsO$_4$, 0.1% uranyl acetate and 3% water in acetone under liquid N$_2$. Freeze substitution was then performed, and sapphire disks embedded in Eponate 12 using the recipe reported previously[6]. Following these manipulations, Epon resin was removed from the bottom side of the sapphire disk, and the disk removed from the resin block by repeated alternating immersion in warm water and liquid N$_2$. The newly exposed Epon surface containing cells was then re-embedded in Durcupan resin.

X-ray correlation and trimming. Samples were then imaged using a micro X-ray CT system (XRadia 510, Carl Zeiss X-ray Microscopy) to identify the positions of the cells of interest. Fluorescence images taken previously were overlaid onto X-ray images to ensure proper ROI location. Specimens were re-mounted on a copper stud and trimmed using an ultramicrotome (EM UC7, Leica Microsystems), with supplementary X-ray CT imaging to guide the trimming process, until the region to be imaged in EM was contained in a resin 'tab' with typical dimensions of approximately 100 × 100 × 65 μm. Finally, samples were sputter-coated with 10 nm gold and 100 nm carbon (PECS 682; Gatan) to maintain sample conductivity for EM.

FIB-SEM. Samples were loaded onto a custom FIB-SEM, consisting of a Zeiss Gemini 450 Field Emission SEM and a Zeiss Capella FIB column oriented at 90 degrees to the SEM beam[46]. Samples were subjected to repeated FIB milling and SEM imaging to acquire 3D EM datasets. Images taken at 8 × 8 × 8 nm pixel resolution were imaged at 500 kHz readout rate, with 1.2 kV landing energy at 2.0 nA electron dose. Milling was performed using a 15 nA gallium ion beam source at 30 kV. Images taken at 4 × 4 × 4 nm^3 pixel resolution were imaged similarly but with

200 kHz readout rate, 0.25 nA electron dose and 0.9 kV landing energy. A pipeline based upon render web services (available at https://github.com/saalfeldlab/render) was used to align and reconstruct the FIB-SEM images into 3D volumes for analysis. Point match correspondences were extracted using SIFT[47], and global optimization[48,49] was employed to compute per-image affine transformations regularized with a rigid model for each entire volume. After alignment, the volumes were flattened using a spline along the z dimension based on key points that were interactively set in BigDataViewer[50].

CLEM registration. Fluorescence and EM image data were co-registered as follows. The mitochondria fluorescence channel (MitoView 650) was manually cropped to approximately match the FOV of the FIB-SEM image. Mitochondria predictions (see 'Automatic ER, mitochondria and PM segmentation in FIB-SEM datasets' section) were downsampled to 64 nm isotropic resolution and coarsely aligned to the cropped light image using BigDataViewer[50]. Resampled predictions were then blurred with a $1 \times 1 \times 3$ pixel Gaussian kernel using Fiji[51]. Processed predictions were registered to the fluorescence image using elastix[52] using two steps. First, we used elastix to estimate an affine transformation between the two volumes. We then ran elastix again, initialized with the estimated affine to find a non-linear transformation. Parameters for both steps can be found at ref. 38. In estimating the non-linear transformation, we provided elastix an automatically generated mask that was non-zero when the image fields of view overlapped. The inverse of the resulting transformation was estimated and applied to all fluorescence images, bringing them into spatial alignment with the FIB-SEM (using code from https://github.com/saalfeldlab/template-building).

Spinning disk confocal microscopy
Microscope. Fluorescence imaging was performed using a Nikon Ti2-E equipped with a Yokogawa CSU-X1 spinning disk unit, LUNF XL laser unit, Nikon Perfect Focus System, Z piezo stage, motorized XY stage, two sCMOS cameras (ORCA-Fusion BT, Hamamatsu Corp.) and two fast filter wheels with most elements controlled through hardware-triggering through Nikon's National Instruments Breakout Box. The acquisition software was NIS-Elements (v5.30.02, v5.30.04 and v5.30.06). The polychroic mirror within the Yokogawa CSU-X1 unit is a Semrock Di01-T405/488/568/647. Single-emission filters (Chroma ET525/36m, Chroma ET605/52m and Chroma ET705/62m) were used with the 488 nm, 561 nm and 640 nm lasers.

Live-cell imaging. For live-cell imaging, cells were seeded on either eight-well chambered #1.5H coverglass (#C8-1.5H-N; Cellvis) or 35 mm #1.5 glass-bottom dishes with four compartments (#627870; Greiner Bio-One). We used a Nikon 100×/1.49 NA Apo TIRF oil immersion objective with its correction collar optimized for our imaging at 37 °C through a #1.5H glass coverslip. Images were taken in 12 bit with high gain ('12-bit Sensitive') and with 'Standard' readout mode. Rough alignment for simultaneous dual-channel imaging was accomplished using 0.1 µm multi-colour TetraSpeck beads to align the Cairn TwinCam unit (holding a Semrock Di02-R561 beamsplitter) until pixel-perfect overlap was achieved in the centre of FOV for the two cameras. Temperature and CO_2 control for maintaining physiological conditions were provided by a Tokai Hit stage top incubation system (model STXF-WELSX-SET). Acquisition settings for figures/experiments are listed in Supplementary Table 2. To accommodate the addition of high-calcium medium during calcium switch experiments, holes were made in polystyrene lids using heated syringes and then sterilized with 70% ethanol.

Image processing
Automatic ER, mitochondria and PM segmentation in FIB-SEM datasets. Segmentations for ER, mitochondria and PM were generated using the 8 nm and 4 nm many-type networks described in ref. 53 for DSM-2 and DSM-3, respectively. With a manual validation Fiji plugin

(available at https://github.com/janelia-cosem/Fiji_COSEM_Predictions_Evaluation), we found the optimal network iterations to be 800k for ER, 875k for mitochondria in DSM-2 (from range 800k–1,000k) and 625k for ER and 750k for mitochondria in DSM-3 (from range 600k–800k). Voxels predicted to belong to organelles were used to segment the organelles into individual connected components[53]. Components smaller than 20×10^6 nm³ were removed. In the case of mitochondria, predictions were first smoothed by a Gaussian kernel ($\sigma = 12$ nm) before connected component analysis.

FIB-SEM image processing (after COSEM predictions). Predicted organelle segmentation results and raw EM data from COSEM/AIC were cropped to remove regions without biologically relevant voxels. Datasets were then re-sliced (rotated) to an orientation akin to typical light microscopy z-stacks. To reduce file sizes, the $4 \times 4 \times 4$ nm³ dataset ('DSM-3') was chopped into 12 tiles of equal dimensions from which one tile containing part of a cell border was selected for segmentation touch-up and analysis. Similarly, 'DSM-2', the $8 \times 8 \times 8$nm³ dataset, was cropped to include only one border. More details about FIB-SEM datasets can be found in Supplementary Table 3.

Keratin intermediate filaments, ribosomes and desmosome outer dense plaque were segmented using the pixel classification workflow from ilastik (v1.3.3). The structure and strong electron density of the outer dense plaque and ribosomes permitted predictions from ilastik to be filtered on the basis of size and intensity with minor manual corrections. If both sides of the outer dense plaque were not available due to sample tearing, these desmosomes were excluded from analysis. Endosomes were frequently misclassified as ER and were re-classified into a separate endosome class. Microscopy Image Browser v2.83 (ref. 54) was used for proofreading segmentation results and manual annotation of microtubules.

Segmentation results were exported from Microscopy Image Browser v2.83 as 3D TIFs and imported into Dragonfly along with the corresponding cropped FIB-SEM dataset. Connected component analysis (26-connection) was done to generate objects of desmosomal outer dense plaque, keratin, microtubules, ER, endosomes and ribosomes, and to classify certain organelles (ER, endosomes, keratin and microtubules) by cell. Sample tearing (from the resin embedding step) resulted in disconnected ER within the same cell, but these objects were manually re-classified as one ER object per cell.

Three-dimensional renderings in Figs. 1–3, Extended Data Figs. 4 and 5, and Supplementary Fig. 1 were generated using Dragonfly software, Version 2022.2 for Windows[55].

FIB-SEM image analysis (after COSEM predictions). To assess the relative location of various organelles on both sides of a desmosome (Fig. 3), unsigned distance transform maps were generated for specific organelles that were split by cell to determine the closest voxel of each organelle to individual desmosomes. To distinguish between smooth and rough ER, we filtered ribosomes on the basis of distance to ER to keep ribosome objects with voxels adjacent to ER. The statistics for the minimum intensity of the unsigned distance transform maps for each desmosome object were exported as comma-separated value files. Desmosomes at locations of sample tearing were excluded from analysis and visualization except for Supplementary Fig. 1.

To compare ER contacts between keratin and microtubules, we used the $4 \times 4 \times 4$ nm³ dataset ('DSM-3') because the $8 \times 8 \times 8$ nm³ dataset ('DSM-2') was insufficient for seeing the hollow tube structure of microtubules. Using Microscopy Image Browser, the ER class was dilated in 3D (by 1–5 voxels, corresponding to 4–20 nm), and then an intermediate filament class was masked with the dilated ER class. Following connected components in 3D with a 26-connected neighbourhood, the objects were exported as .csv files and plotted using seaborn (v0.12.0) and matplotlib (3.7.1) (refs. 56–59).

Fluorescence microscopy image processing. Images were split by channels and timepoints before denoising with either Noise2Void[60] or 3DRCAN (Supplementary Fig. 4)[61]. After re-combining to a hyperstack, all datasets were corrected for lateral chromatic aberration using NanoJ's channel registration[62]. If needed, images were then drift corrected using NanoJ's drift correction. Fiji/ImageJ macros are provided at ref. [38].

3DRCAN. A431 cells stably expressing mApple-VAPB were grown on #1.5 glass coverslips and fixed using 2% paraformaldehyde for 15 min at 37 °C before being mounted in ProLong Gold and left to cure for 72 h. Acquisition settings for the low signal-to-noise ratio (SNR) images were chosen to match the SNR during live-cell imaging. The high SNR settings used higher laser power and higher exposure to compensate for the fixation-induced loss in fluorescence. 'Ground truth' datasets were obtained after Richardson–Lucy deconvolution of the high-SNR datasets. After excluding datasets that showed focal drift between the low-/high-SNR datasets, we had 37 (34 training and 3 validation) datasets. Training parameters can be found in Supplementary Table 4. A Windows 10 workstation with an NVIDIA RTX 3090 graphics processing unit (GPU) was used.

Noise2Void and N2V2. Noise2Void v0.2.1 was used with TensorFlow-DirectML on a Windows 10 workstation with an NVIDIA RTX 3090 GPU. Compared with Noise2Void, N2V2 yielded superior results in our FIB-SEM datasets by improving denoising quality and reducing chequerboard artefacts[63]. N2V2 training and prediction was done through the napari-n2v plugin on napari[64]. In some cases, N2V training and prediction used the N2V CSBDeep Fiji plugin on a Windows 10 workstation with an NVIDIA Quadro RTX 4000 GPU. Training parameters can be found in Supplementary Tables 5 and 6.

Image analysis
Segmentation with ilastik and generation of overlapping signals. To determine the extent of co-localization between DP or KRT14[R125C] aggregates and VAPB over time, we performed an analysis of overlapping signals (Fig. 4c and Extended Data Fig. 10i). We first generated binary masks of DP-EGFP, KRT14[R125C] aggregates and mApple-VAPB channels using the Pixel Classification workflow in ilastik[65]. Briefly, features were drawn to differentiate foreground from background pixels in denoised images. This step generates a binary image for each channel, with true signal value of 1 and background value of 0. Additionally, in ilastik-segmented KRT14[R125C] images, any keratin filamentous structures present were cleared using Fiji so that only keratin aggregates were analysed.

To generate an overlap image, we used Fiji[51] to perform a 'Multiply' calculation on ilastik-segmented binary masks of DP or KRT14[R125C] images and the corresponding VAPB images. Therefore, only non-zero pixels in both channels are kept. These resulting pixels suggest co-localization between DP puncta (desmosomes) or KRT14[R125C] aggregates and VAPB (ER) at the resolution limit of standard spinning disk confocal microscopy.

Analysis of DP-VAPB co-localization. Fiji macros were developed to determine whether DP puncta exhibited interactions with ER membrane over a 2 min duration with image acquisition every 5 s (25 timepoints) (Fig. 4c). Briefly, we drew ROIs around individual ilastik-segmented DP puncta to obtain information about puncta position and area. Only DP puncta that remained in focus for all 25 timepoints and that were equal to or larger than 4 pixels were selected for analysis. These ROI positions were then applied to the corresponding 'Multiplied' image file (see 'Segmentation with ilastik and generation of overlapping signals' section) to acquire area measurements at each timepoint. An area value of <4 pixels meant no overlap between a DP ROI and ER membrane for that timepoint.

Analysis of co-localization between KRT14[R125C] aggregates and VAPB. Fiji macros were developed to determine whether KRT14[R125C] aggregates co-localized with ER membrane over a 2 min duration with image acquisition every 5 s (25 timepoints) (Extended Data Fig. 10i). Briefly, we used the 'Analyze Particles' function in Fiji to generate ROIs of ilastik-segmented KRT14[R125C] aggregates to obtain information about puncta position and area. Only KRT14[R125C] aggregates that were at least 4 pixels were selected for analysis. These ROI positions were then applied to the corresponding 'Multiplied' image file (see 'Segmentation with ilastik and generation of overlapping signals' section) to acquire area measurements for each ROI at each timepoint. An area value of <4 pixels meant no overlap between a KRT14[R125C] aggregate ROI and ER membrane for that timepoint.

MDA. To quantify the displacement of ER membranes at various cellular locations and between conditions, we calculated optical flow fields and classified membrane movement as either static or mobile using a modified version of a previously published Fiji macro[14]. We performed MDA on ROIs of 35 pixels × 35 pixels (2.275 μm × 2.275 μm) with the following parameters for MSEGaussianFlow: sigma 4, maximal_distance 10. The extent of membrane movement was depicted by the pixel intensity, with higher movement between frames corresponding to higher intensity values. ER membrane movement was classified into two categories based on the amount of movement in pixels: 'Static ER' (0–2 pixels) or 'Mobile ER' (3–9 pixels). Masking of the mApple-VAPB channel was performed using the 'Percentile' thresholding in Fiji. The MSEGaussianFlow plugin was authored by Stephan Saalfeld and Pavel Tomancak.

qRT–PCR analysis
RNA was isolated from cells using TRIzol (Invitrogen) and purified by chloroform extraction. RNA concentration and purity were assessed by spectrophotometry. A total of 200–400 ng of RNA was reverse transcribed using the iScript cDNA Synthesis Kit (1708891; Bio-Rad Laboratories). Two technical replicates were performed for all samples.

For expression analysis of K14[WT]- and K14[R125C]-expressing A431 cells, qRT–PCR was performed using TaqMan Fast Advanced Master Mix (4444557; Applied Biosystems) and Light Cycler 480 (Roche). TaqMan MGB probes labelled with fluorescent dyes were used. Reaction was performed according to the following protocol: 50 °C for 2 min, 95 °C for 20 s, and (50 cycles of 95 °C for 3 s and 60 °C for 30 s). Probes against specific genes were labelled with the FAM dye. *TBP* was labelled with the VIC dye and used as the reference gene within the same tube as the gene of interest. Normalized expression was calculated using Microsoft Excel (version 2303) by subtracting the cycle threshold (C_t) values of the internal control gene from the C_t value of the gene of interest, followed by averaging this value across all technical replicates. Fold change relative to K14[WT] cells was then calculated by the $2^{-\Delta\Delta Ct}$ method. More details about TaqMan probes are provided in Supplementary Table 7.

For expression analysis of cells treated with normal human IgG or PV IgGs, qRT–PCR was performed using the PerfeCta SYBR Green (101414-272; Quanta Biosciences) and Light Cycler 480 (Roche). Reaction was performed according to the following protocol: 95 °C for 3 min, and 45 cycles of (95 °C for 5 s and 60 °C for 30 s). *RPLPO* and *TBP* were used as reference genes. Normalized expression was calculated in Microsoft Excel by averaging the C_t values across all technical replicates and then normalizing to the geometric mean of the average C_t values of *RPLPO* and *TBP*. Fold change relative to normal human IgG control was then calculated by the $2^{-\Delta\Delta Ct}$ method. Primer sequences are provided in Supplementary Table 8.

Normalized expression for each target gene was determined from at least three biological replicates. Error bars represent standard error of the mean (s.e.m.) of ΔΔCt values.

Statistics and reproducibility

Sample sizes were chosen on the basis of past experience in the lab and previous studies. No pre-determined tests were performed to calculate sample size. The cells used for live-cell experiments were stable immortalized/transformed cell lines that were not clonally selected and therefore represented a population. All experiments were repeated at least three times, unless specified otherwise in the legends, and similar results were obtained in all replicates. DMSO control for thapsigargin and nocodazole treatment experiments (Fig. 5 and Extended Data Figs. 7 and 9) were performed at least twice. TEM was performed on cultured human cells and two different rat organ systems (skin and gut tissue). Western blot was repeated twice, and similar results were obtained. Samples sizes for FIB-SEM datasets were limited by long acquisition times and sample preparation, and the need for accurate segmentation in these large datasets. Therefore, measurements were obtained for one cell–cell contact each from the DSM-2 (8 nm) and DSM-3 (4 nm) datasets.

Some desmosomes in the FIB-SEM datasets were excluded because of sample tearing or because only part of the desmosome was contained within the cropped datasets. Live-cell datasets were excluded if there was substantial sample drift. For calcium switch experiments, datasets were excluded if two or more cells did not form cell–cell contacts. The Investigators were not blinded to allocation during experiments and outcome assessment.

For live-cell imaging experiments, cells expressing fluorescent constructs were seeded into wells and image fields were selected on the basis of two criteria: (1) two or more adjacent cells expressing the fluorescent constructs were in the same field, and (2) adjacent cells had similar fluorescence intensity levels. Covariates were controlled by maintaining all samples in the same growth conditions on the same dish (in different wells), until addition of drug or DMSO. For the CLEM experiments, regions were chosen for FIB-SEM acquisition using the results of Cryo-SIM imaging with the following conditions for all cells within the ROIs: (1) similar expression levels of mApple-VAPB and DP-EGFP, and (2) healthy/normal morphology. Further cropping of FIB-SEM datasets was necessary for analysis due to computer hardware constraints and segmentation requirements. The cropped regions for analysis were chosen because they contained desmosomes without being greatly impacted by sample tearing.

Statistical testing was performed using R (version 4.2.3) (Figs. 4f and 7f) or Prism 8 (GraphPad Software) (Fig. 8l,m). Exact P values are provided. Normality testing was first performed with the D'Agostino-Pearson omnibus (K2) test. When normality tests failed, statistical significance was calculated using the non-parametric Mann–Whitney test.

Reporting summary

Further information on research design is available in the Nature Portfolio Reporting Summary linked to this article.

Data availability

All macros and plasmid maps are available at https://doi.org/10.5281/zenodo.6800360 (ref. 38). FIB-SEM datasets are hosted on https://www.openorganelle.org/datasets/aic_desmosome-2 and https://www.openorganelle.org/datasets/aic_desmosome-3. Other imaging source data, including spinning disk confocal microscopy data, are hosted on ScholarSphere (https://doi.org/10.26207/53vq-g344). Source data are provided with this paper. All other data supporting the findings of this study are available from the corresponding author on reasonable request.

Code availability

All code and macros are available at https://doi.org/10.5281/zenodo.6800360.

References

36. Kremers, G.-J., Hazelwood, K. L., Murphy, C. S., Davidson, M. W. & Piston, D. W. Photoconversion in orange and red fluorescent proteins. *Nat. Methods* **6**, 355–358 (2009).
37. García-Nafría, J., Watson, J. F. & Greger, I. H. IVA cloning: a single-tube universal cloning system exploiting bacterial in vivo assembly. *Sci. Rep.* **6**, 27459 (2016).
38. KowalczykLab/Desmosome-ER/. *Zenodo* https://doi.org/10.5281/zenodo.6800360 (2023).
39. Calkins, C. C. et al. Desmoglein endocytosis and desmosome disassembly are coordinated responses to pemphigus autoantibodies. *J. Biol. Chem.* **281**, 7623–7634 (2006).
40. Schell, S. L. et al. Keratinocytes and immune cells in the epidermis are key drivers of inflammation in hidradenitis suppurativa providing a rationale for novel topical therapies. *Br. J. Dermatol.* **00**, 1–13 (2022).
41. Baddam, S. et al. The desmosomal cadherin desmoglein-2 experiences mechanical tension as demonstrated by a FRET-based tension biosensor expressed in living cells. *Cells* **7**, 66 (2018).
42. Tsunoda, K. et al. Induction of pemphigus phenotype by a mouse monoclonal antibody against the amino-terminal adhesive interface of desmoglein 3. *J. Immunol.* **170**, 2170–2178 (2003).
43. Saito, M. et al. Signaling dependent and independent mechanisms in pemphigus vulgaris blister formation. *PLoS ONE* **7**, 50696 (2012).
44. Stahley, S. N. et al. Super-resolution microscopy reveals altered desmosomal protein organization in tissue from patients with pemphigus vulgaris. *J. Invest. Dermatol.* **136**, 59–66 (2016).
45. Gustafsson, M. G. et al. Three-dimensional resolution doubling in wide-field fluorescence microscopy by structured illumination. *Biophys. J.* **94**, 4957–4970 (2008).
46. Xu, C. S. et al. Enhanced FIB-SEM systems for large-volume 3D imaging. *eLife* **6**, e25916 (2017).
47. Lowe, D. G. Distinctive image features from scale-invariant keypoints. *Int. J. Comput. Vis.* **60**, 91–110 (2004).
48. Saalfeld, S., Fetter, R., Cardona, A. & Tomancak, P. Elastic volume reconstruction from series of ultra-thin microscopy sections. *Nat. Methods* **9**, 717–720 (2012).
49. Preibisch, S., Saalfeld, S. & Tomancak, P. Globally optimal stitching of tiled 3D microscopic image acquisitions. *Bioinformatics* **25**, 1463 (2009).
50. Pietzsch, T., Saalfeld, S., Preibisch, S. & Tomancak, P. BigDataViewer: visualization and processing for large image data sets. *Nat. Methods* **12**, 481–483 (2015). *2015 12:6*.
51. Schindelin, J. et al. Fiji: an open-source platform for biological-image analysis. *Nat. Methods* **9**, 676–682 (2012).
52. Klein, S., Staring, M., Murphy, K., Viergever, M. A. & Pluim, J. P. W. Elastix: a toolbox for intensity-based medical image registration. *IEEE Trans. Med. Imaging* **29**, 196–205 (2010).
53. Heinrich, L. et al. Whole-cell organelle segmentation in volume electron microscopy. *Nature* **599**, 141–146 (2021).
54. Belevich, I., Joensuu, M., Kumar, D., Vihinen, H. & Jokitalo, E. Microscopy Image Browser: a platform for segmentation and analysis of multidimensional datasets. *PLoS Biol.* **14**, e1002340 (2016).
55. Dragonfly 2020.2. *Object Research Systems* http://www.theobjects.com/dragonfly (2020).
56. Waskom, M. L. seaborn: statistical data visualization. *J. Open Source Softw.* **6**, 3021 (2021).
57. pandas-dev/pandas: Pandas (v1.5.3). *Zenodo* https://doi.org/10.5281/ZENODO.7549438 (2023).

58. McKinney, W. Data structures for statistical computing in Python. In *Proc. 9th Python in Science Conference* (eds van der Walt, S. & Millman, J.) 56–61 (2010).

59. Hunter, J. D. Matplotlib: a 2D graphics environment. *Comput. Sci. Eng.* **9**, 90–95 (2007).

60. Krull, A., Buchholz, T. O. & Jug, F. Noise2void-Learning denoising from single noisy images. In *Proc. 2019 IEEE/CVF Computer Society Conference on Computer Vision and Pattern Recognition* 2124–2132 (IEEE, 2019).

61. Chen, J. et al. Three-dimensional residual channel attention networks denoise and sharpen fluorescence microscopy image volumes. *Nat. Methods* **18**, 678–687 (2021).

62. Laine, R. F. et al. NanoJ: a high-performance open-source super-resolution microscopy toolbox. *J. Phys. D* **52**, 163001 (2019).

63. Höck, A. F. E., Buchholz, T.-O., Brachmann, A. & Jug, F. N2V2—fixing Noise2Void checkerboard artifacts with modified sampling strategies and a tweaked network architecture. In *Computer Vision – ECCV 2022 Workshops. ECCV 2022. Lecture Notes in Computer Science,* Vol. 13804 (eds Karlinsky, L. et al.) 503–518 (Springer, 2022).

64. Sofroniew, N. et al. napari: a multi-dimensional image viewer for Python (v0.4.16). *Zenodo* https://doi.org/10.5281/ZENODO.7276432 (2022).

65. Berg, S. et al. ilastik: interactive machine learning for (bio)image analysis. *Nat. Methods* **16**, 1226–1232 (2019).

Acknowledgements

Author contributions

N.K.B., S.N.S. and A.P.K. were involved with project conception. N.K.B. and A.P.K. wrote the manuscript with input from all co-authors. N.K.B. and W.G. were involved with experimental design, image acquisition and analysis, writing the methods section and making figures and movies. N.K.B. and C.L.H. performed qRT–PCR analysis. T.-L.C. supervised Cryo-SIM and FIB-SEM workflow. J.S.A. was involved with cryogenic light microscopy image acquisition/processing and FIB-SEM data acquisition. S.K. was involved with Cryo-SIM/FIB-SEM sample preparation including cell culture/labelling, high-pressure freezing and sample trimming. COSEM Project Team, S.S. and A.V.W. supervised ER segmentation in FIB-SEM datasets. S.P., E.T.T. and D.B. were involved with FIB-SEM data pre-processing. D.B. and E.T.T. organized FIB-SEM data and data attributes. W.P. and A.P. provided manual annotations, evaluations and proofreading. D.B. built the data management infrastructure. L.H. and S.S. developed machine learning algorithms; L.H. performed network training and predictions. D.A. and S.S. developed refinement and analysis algorithms; D.A. analysed data. J.B. and S.S. developed automated CLEM registration algorithms; J.B. performed automated CLEM registration. A.W.V. was involved with transmission EM acquisition in Extended Data Fig. 2. A.P.K. and S.N.S. were involved with funding acquisition. A.P.K. supervised the project.

Competing interests

The authors declare no competing interests.

Additional information

Extended data is available for this paper at https://doi.org/10.1038/s41556-023-01154-4.

Supplementary information The online version contains supplementary material available at https://doi.org/10.1038/s41556-023-01154-4.

**Correspondence and requests for materials** should be addressed to Andrew P. Kowalczyk.

Peer review information *Nature Cell Biology* thanks Edward Avezov and the other, anonymous, reviewer(s) for their contribution to the peer review of this work. Peer reviewer reports are available. Peer reviewer reports are available.

Reprints and permissions information is available at www.nature.com/reprints.
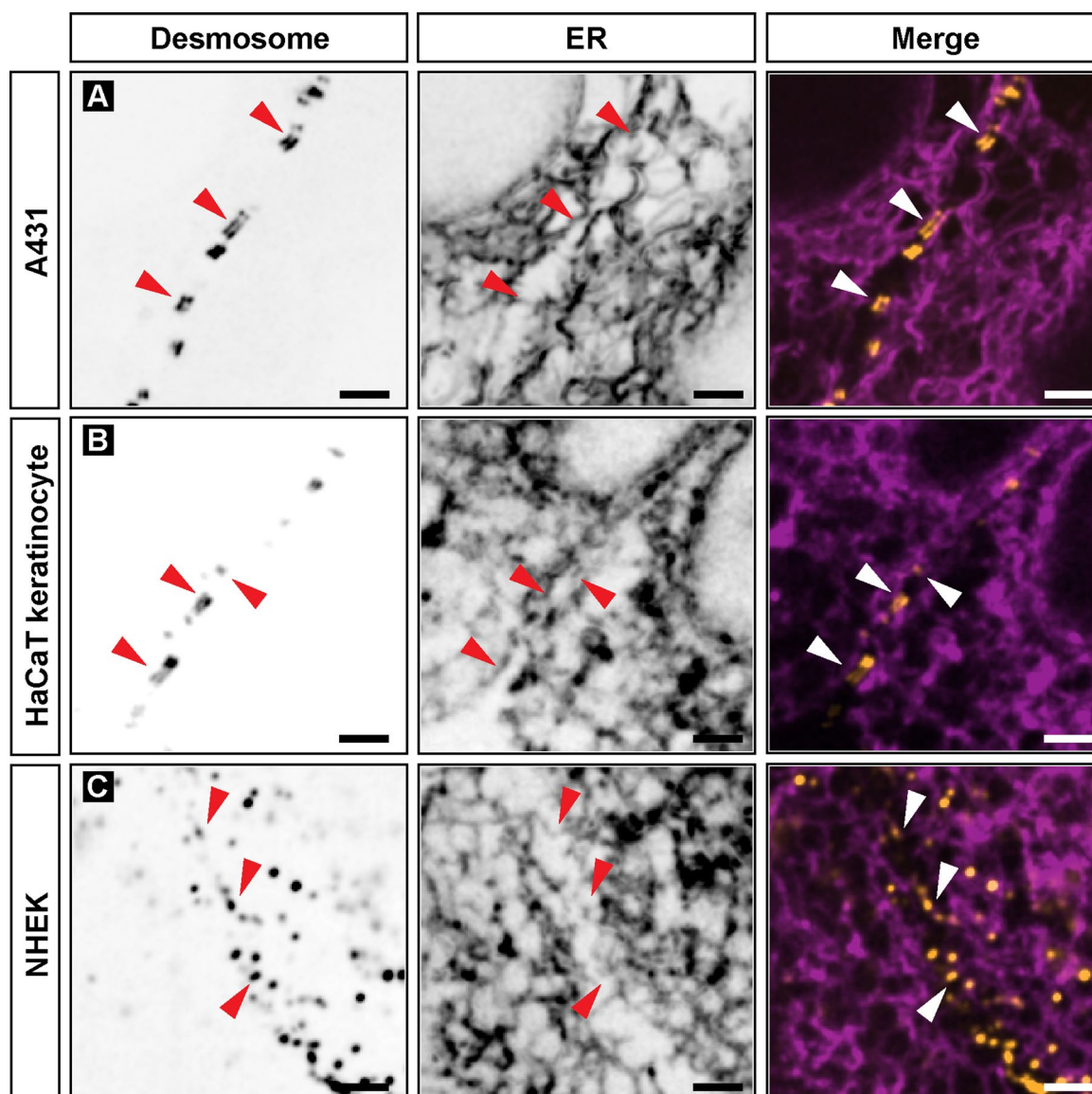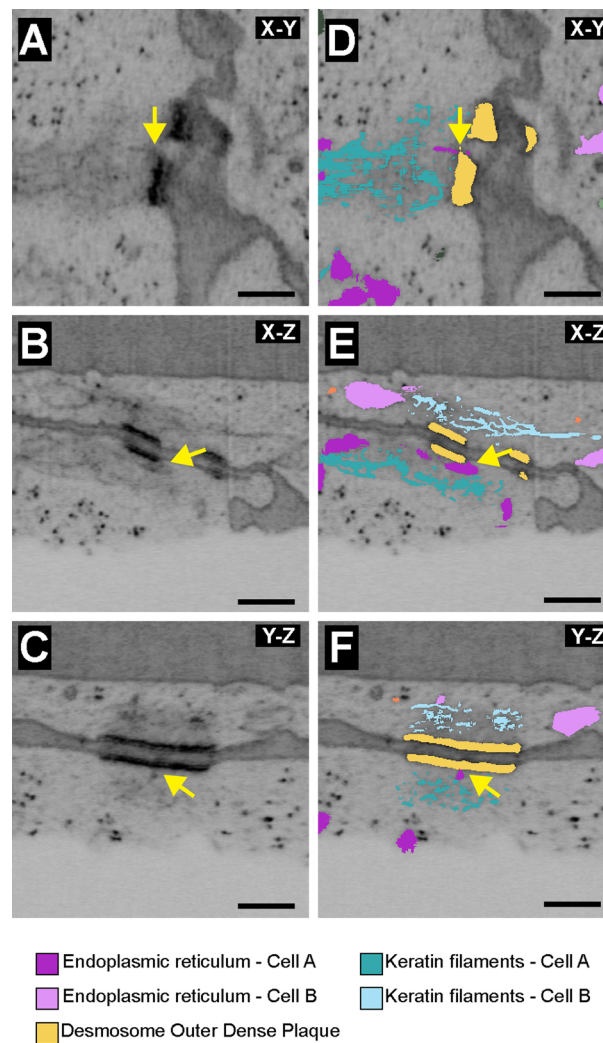
Extended Data Fig. 1 | ER tubules are proximal to desmosomal junctions in various epithelial cell culture models. (a–c) Representative light microscopy images of a pair of A431 cells (**A**), HaCaT immortalized keratinocytes (**B**), and primary normal human epidermal keratinocytes (**C**) expressing mCherry-VAPB (magenta, ER marker) showing ER tubule and desmosomal junction (orange) proximity (red or white arrowheads). Desmosomes are labelled with DP-EGFP in **A** and **B**, or with an Alexa Fluor 488 conjugated anti-DSG3 mAb (AK23) in **C**. Images are representative of n = 3 independent experiments (**A, B**) and 2 independent experiments (**C**). Scale bar = 2μm.
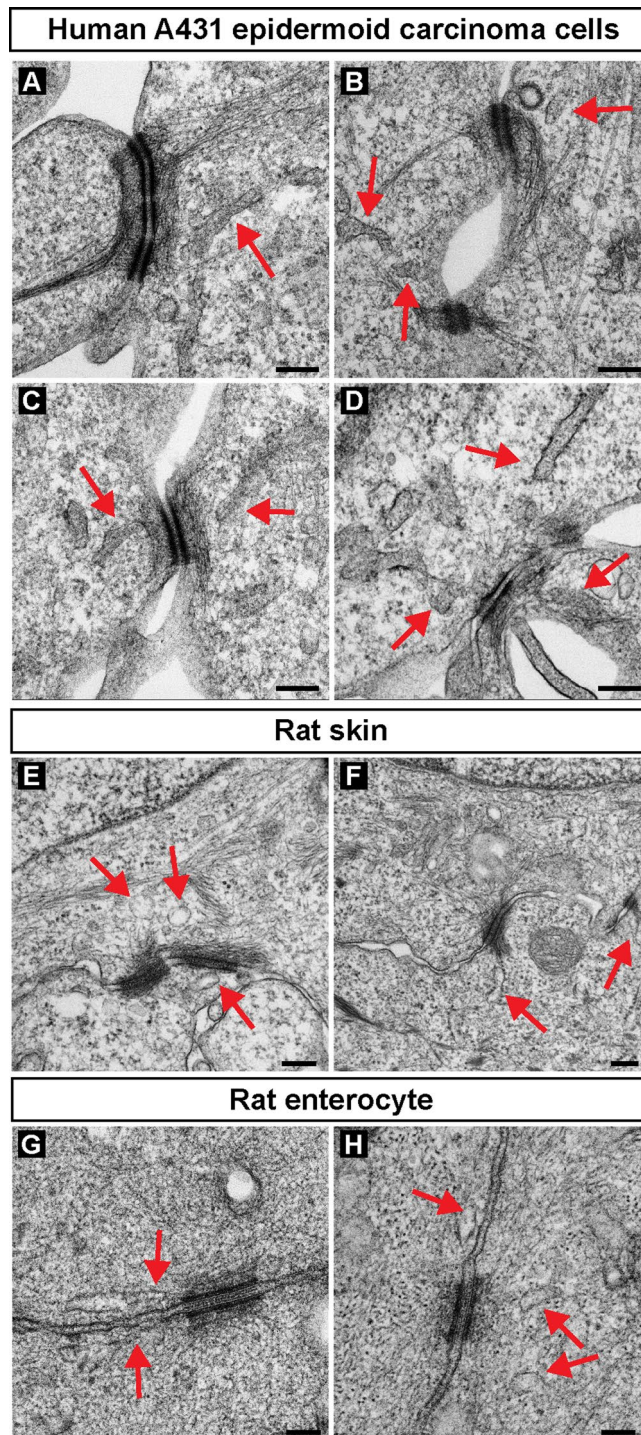
Extended Data Fig. 2 | ER tubules are proximal to the desmosomal plaque in epithelial cell culture models and various tissues. (**a-h**) Transmission electron micrographs of A431 epithelial cells (**A-D**), rat skin (**E, F**), and rat enterocytes (**G, H**) show ER tubules (red arrows) proximal to the electron-dense desmosomal plaque. Images are representative of n = 1 replicate for each cell or tissue type. Scale bar = 200 nm (**A-F**), 100 nm (**G, H**).

■ Endoplasmic reticulum - Cell A   ■ Keratin filaments - Cell A
■ Endoplasmic reticulum - Cell B   ■ Keratin filaments - Cell B
■ Desmosome Outer Dense Plaque

Extended Data Fig. 3 | FIB-SEM reveals ER tubules in physical contact with the desmosome outer dense plaque. (a–c) Orthoslices in XY (**A**), XZ (**B**), and YZ (**C**) showing ER tubules making physical contact with desmosome outer dense plaque. (**d**–**f**) Same orthoslices as in **A-C** with ER, keratin, and desmosome segmentations. Yellow arrows point to physical contact between ER tubules and the desmosome outer dense plaque in all 3 views. Images are representative of n = 1 cell-cell contact. Scale bar = 250 nm.

Endoplasmic reticulum - Cell A   Keratin filaments - Cell A
Endoplasmic reticulum - Cell B   Keratin filaments - Cell B
Microtubules - Cell A   Desmosome Outer Dense Plaque
Microtubules - Cell B   Ribosomes
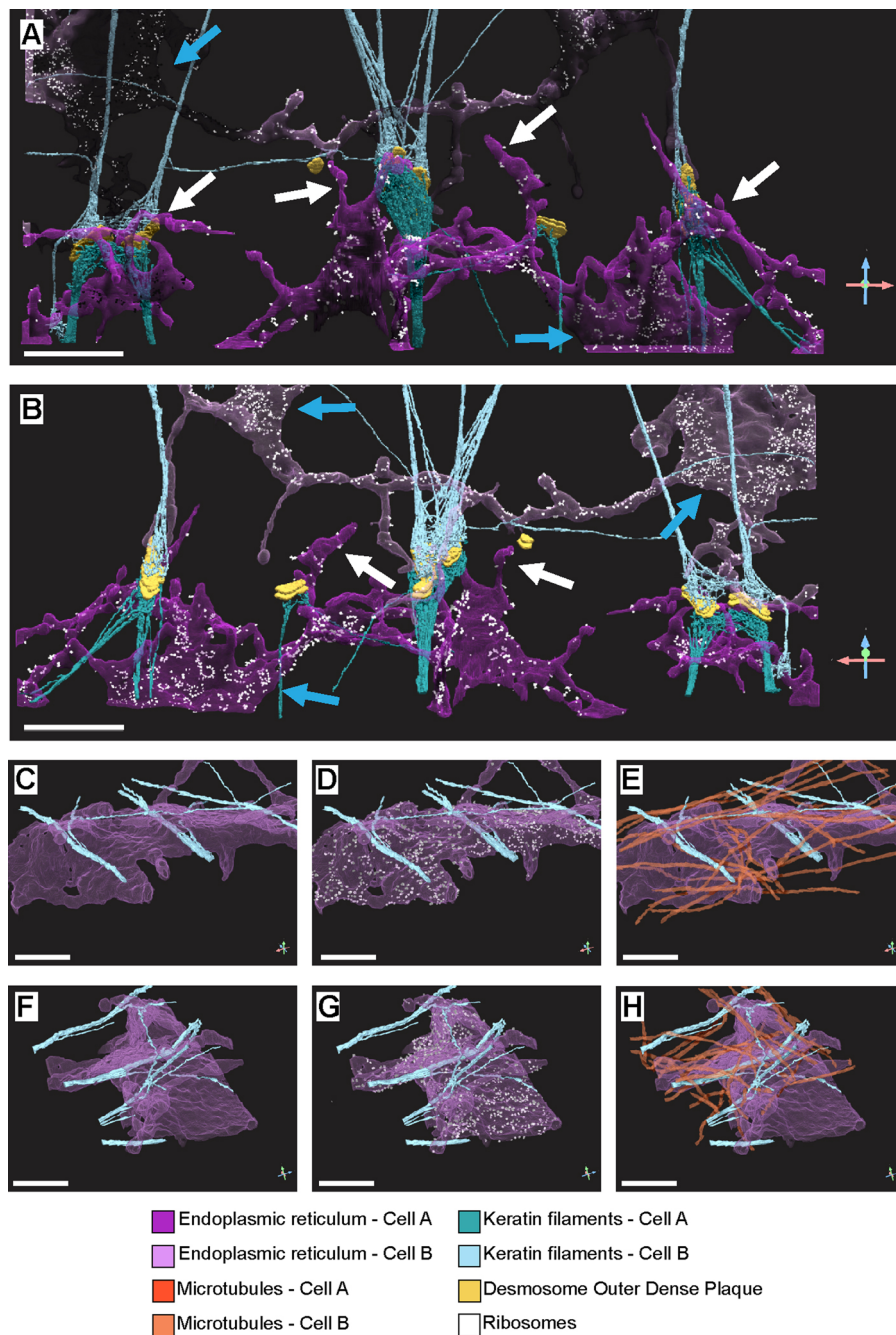
Extended Data Fig. 4 | Ribosomes are less prominent on desmosome-adjacent ER than planar ER. (a, b) Rotated views showing that ER structures (magenta) have fewer bound ribosomes (white) at desmosome (yellow)-adjacent regions (white arrows) than at regions further away from the desmosome (blue arrows) in both top and bottom cells. Images are representative of n = 1 cell-cell contact. Scale bar = 1μm. **(c–e)** Three-dimensional reconstructions of segmentations in 4 × 4 × 4nm³ FIB-SEM data reveal keratin filaments (teal) contacting and penetrating planar ER sheets (magenta). Microtubules (orange) are also present in the vicinity of planar ER, and ribosomes (white) decorate the surface of ER sheets. **(f–h)** Rotated views of the same region in **C-E**. Images are representative of n = 1 cell. Scale bar = 500 nm **(C-H)**.
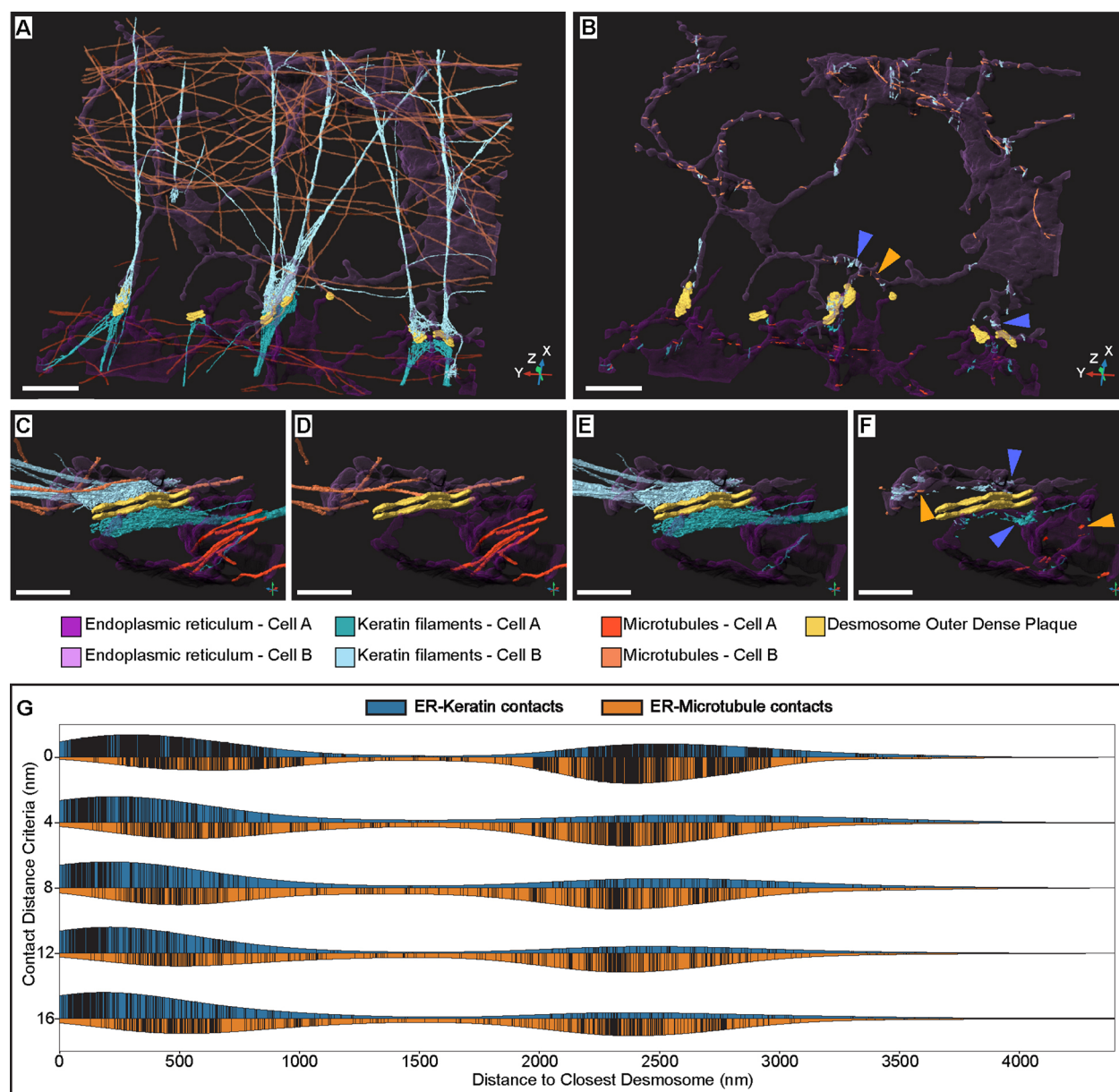
Extended Data Fig. 5 | The ER makes more contacts with keratin filaments compared to microtubules proximal to the desmosome. (a–b) FIB-SEM segmentations showing keratin filaments (teal), desmosomes (yellow), microtubules (orange), and ER (magenta) (**A**). Panel (**B**) displays ER-keratin (teal) and ER-microtubule (orange) contacts at a distance threshold of 16 nm. Scale bar = 1μm. (**c–f**) Close-up of keratin filaments, microtubules, and ER adjacent to a desmosome (**C-E**) revealing larger and more numerous ER-keratin contacts (blue arrowheads) compared to ER-microtubule contacts (orange arrowheads) (**F**). Images in **A-F** are representative of n = 1 cell-cell contact. Scale bar = 500 nm. (**g**) Violin plots of ER-keratin (blue) and ER-microtubule (orange) contacts at x nm away from the closest desmosome. Individual contacts are represented by black vertical lines. Setting various contact site distance thresholds between 0 nm to 16 nm (y-axis) demonstrates that ER-keratin contacts preferentially occur proximal to desmosomes. Source numerical data are available in source data.
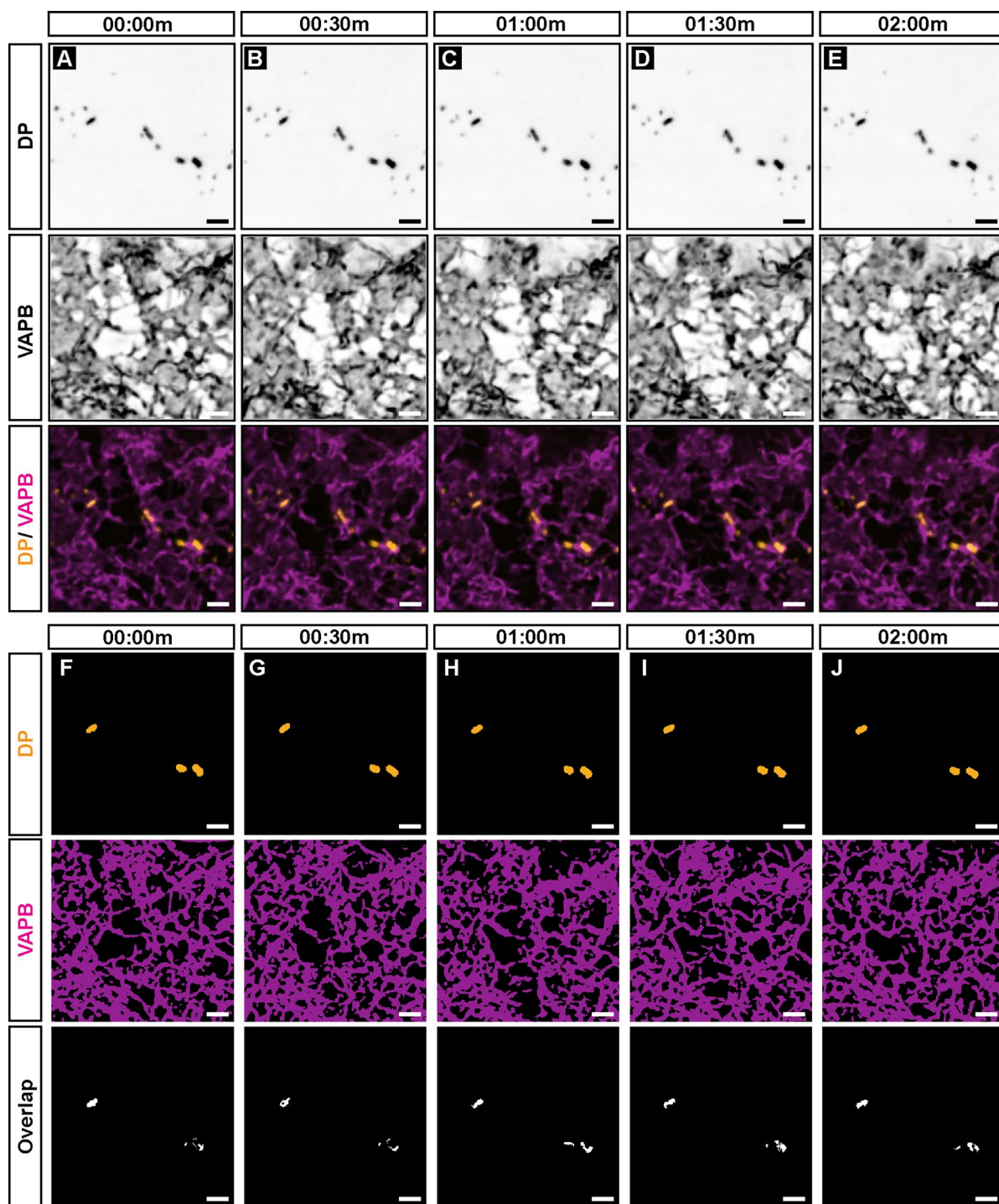
Extended Data Fig. 6 | ER tubules closely associate with desmosomes in live cells. (**a**–**e**) Snapshots of a live-cell time-course of Desmoplakin-EGFP (DP) (top row, orange in bottom row) and mApple-VAPB (middle row, magenta in bottom row) in A431 cells at the cell-cell contact over 2 minutes (Images are representative of n = 3 independent experiments). Gamma correction was applied to grayscale images. Gamma (inverted) = 1.5 (VAPB). Scale bar = 2µm. (**f**–**j**) ilastik-segmentations of DP (top row) and VAPB (middle row) channels in **A-E**. Bottom row indicates overlapping pixels (white) between DP and VAPB channels. Overlap indicates that tips of ER tubules colocalize with DP puncta. Scale bar = 2µm.
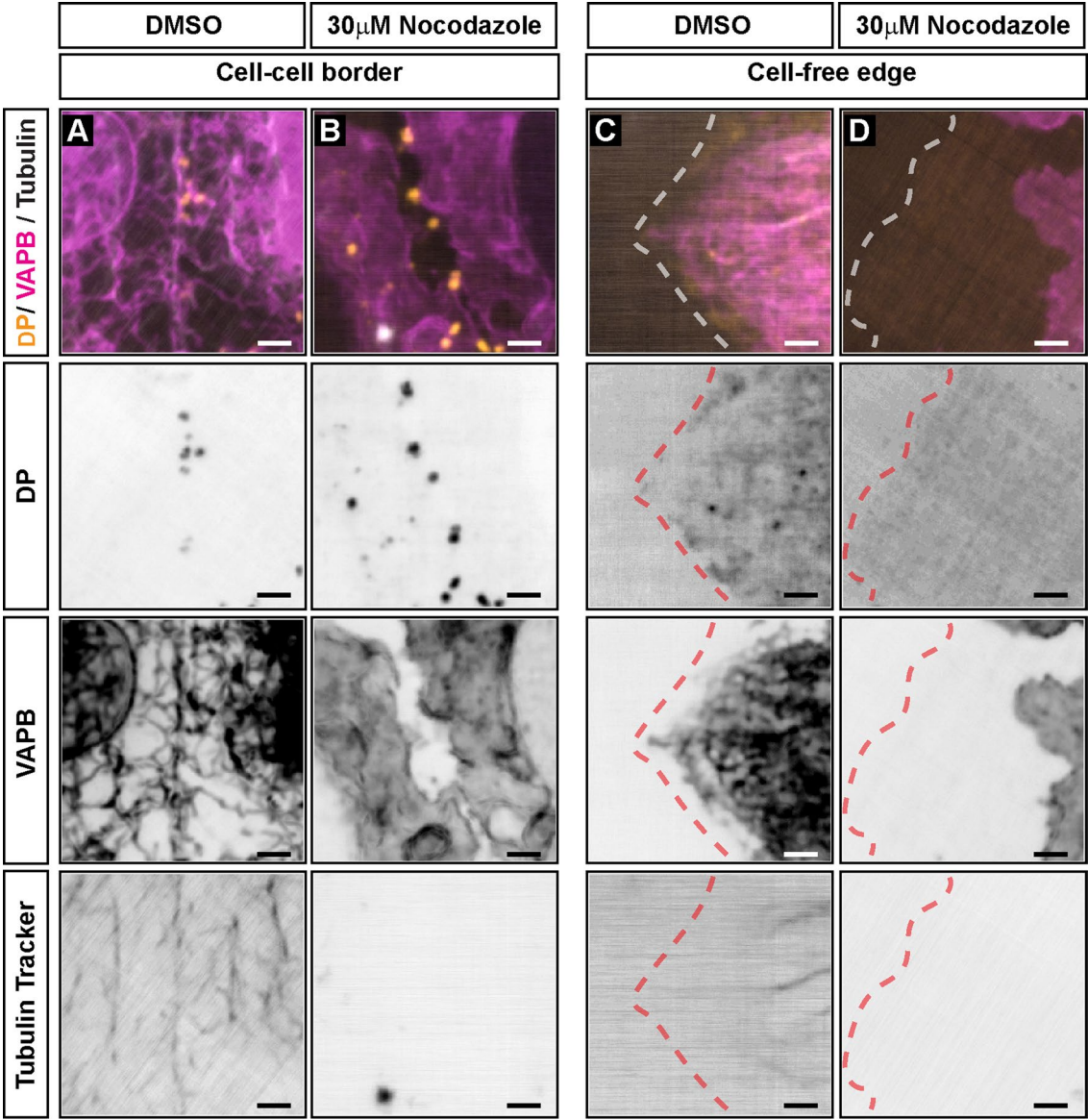
Extended Data Fig. 7 | ER retracts from cell-free edges only in cells where microtubules are depolymerized. (**a**, **b**) Representative images of A431 cells treated with either DMSO or 30μM nocodazole reveal that ER (VAPB, magenta) tubules are converted to sheets with nocodazole treatment. The ER remains tethered to desmosomes (DP, orange) at cell-cell contacts under both treatment conditions. Images are representative of at least n = 2 independent experiments. Scale bar = 2μm. (**c**, **d**) Representative images of A431 cells treated with either DMSO or 30μM nocodazole reveal that ER (VAPB, magenta) remains close to the periphery of a cell-free edge in DMSO-treated cells (**C**) but retracts in nocodazole-treated cells (**D**). Tubulin Tracker Deep Red labelling reveals a lack of microtubules in nocodazole-treated cells but not in DMSO-treated cells. Cell-free edge is depicted by a dashed red or white line. Images are representative of at least n = 2 independent experiments. Scale bar = 2μm. Gamma correction was applied to some grayscale images. Gamma (inverted) = 1.75 (**D**, DP channel), 0.75 (**A**, Tubulin Tracker channel), 1.5 (**C**, Tubulin Tracker channel).
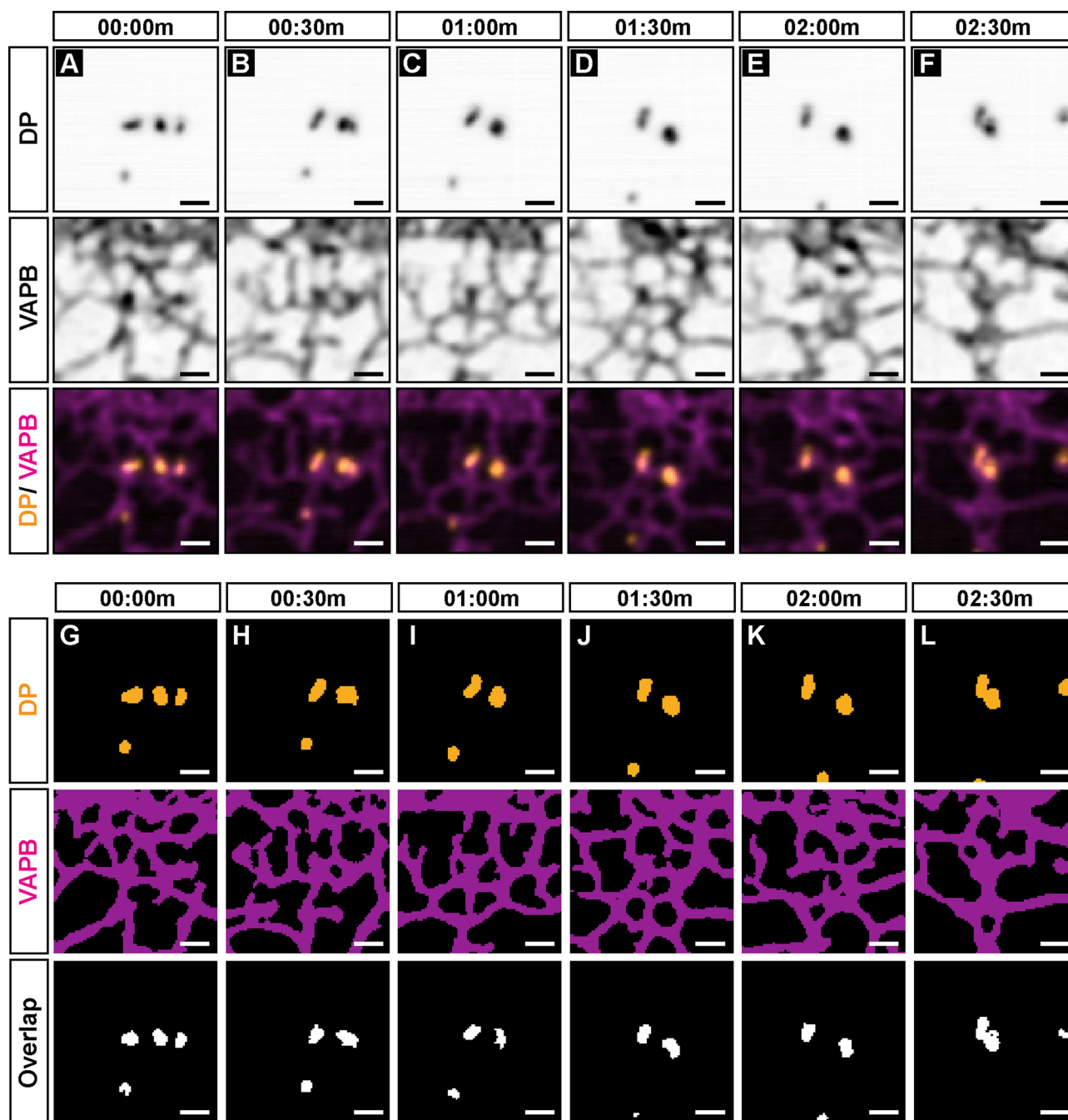
Extended Data Fig. 8 | ER tubules associate with desmosomes during fusion events. (a–f) Snapshots of a live-cell time-course of desmoplakin (top row, orange in bottom row) and VAPB (middle row, magenta in bottom row) in A431 cells during the fusion of DP puncta at the cell-cell contact (Images are representative of n = 4 independent experiments). Three DP puncta (**A**) fuse to form two puncta (**B**). Eventually, these puncta fuse to form one DP puncta (**F**).

Gamma correction was applied to grayscale images. Gamma = 0.7 (DP/VAPB merge), Gamma (inverted) =1.5 (VAPB). Scale bar = 1μm. (**g–l**) ilastik-segmentations of DP (top row) and VAPB (middle row) channels in A-F. Bottom row indicates overlapping pixels (white) between DP and VAPB channels. Overlap indicates that tips of ER tubules colocalize with DP puncta during fusion. Scale bar = 1μm.
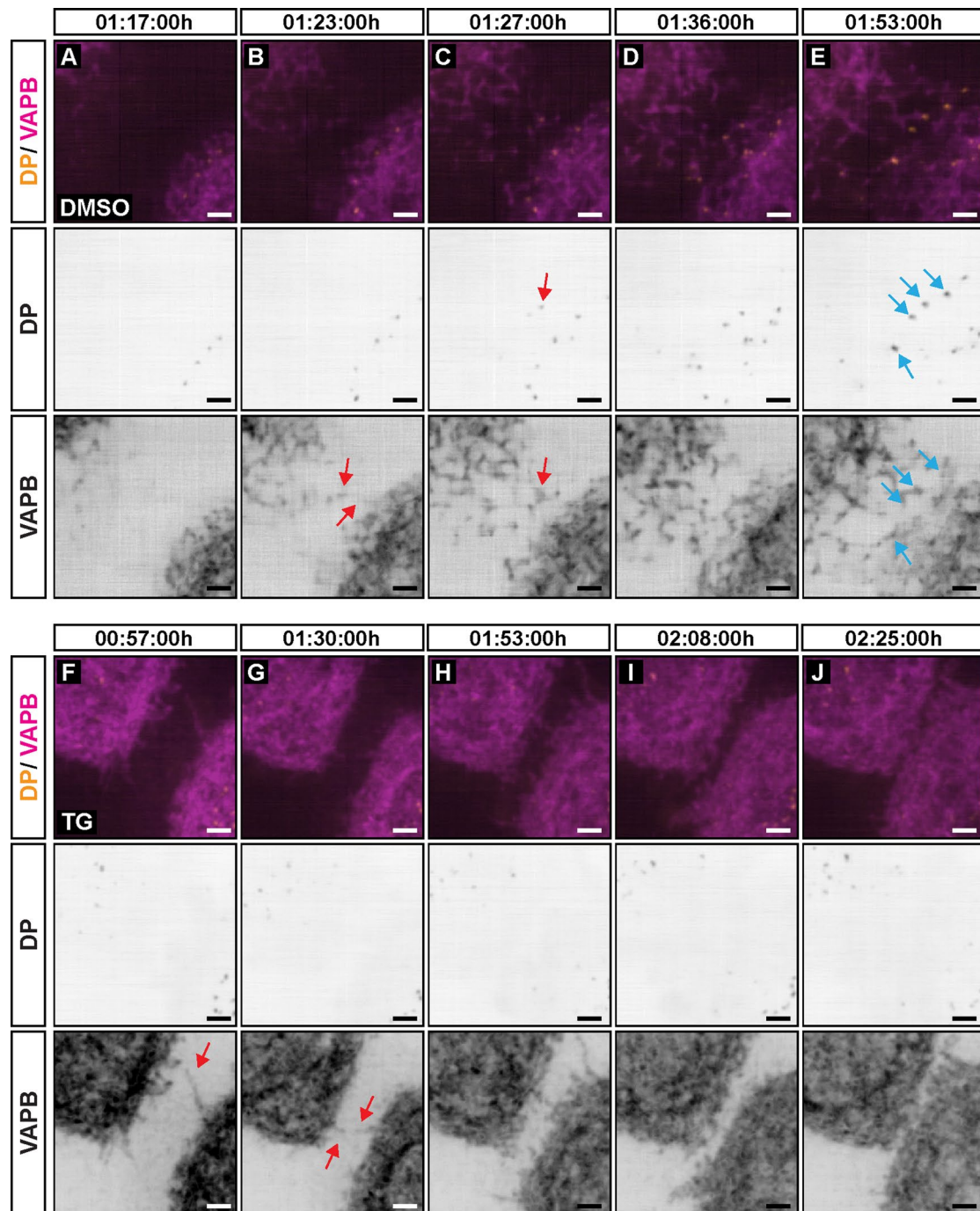
Extended Data Fig. 9 | ER tubules remain at the cell-cell border even when desmoplakin translocation to the border is inhibited. (a–e) Representative time-lapse of A431 cells expressing DP-EGFP (orange) and mApple-VAPB (magenta) pre-treated with DMSO for 30 minutes, followed by a switch to high calcium media. ER tubules extend toward the cell periphery, sometimes forming paired structures across adjacent cells (red arrows, **B**). Desmosomes form at the exact position of ER paired structures (blue arrows in **E**). Images are representative of n = 2 independent experiments. Scale bar = 2μm.

(f–j) Representative time-lapse of A431 cells expressing DP-EGFP (orange) and mApple-VAPB (magenta) pre-treated with 1μM thapsigargin (TG) for 30 minutes, followed by a switch to high calcium media. ER tubules extend toward the cell periphery, sometimes forming paired structures across adjacent cells (red arrows, **F**, **G**). ER tubules eventually remain at the periphery in adjacent cells, but no desmosomes form (**J**). Timestamps indicate time after DMSO/thapsigargin wash-out and switch to high calcium media. Images are representative of n = 3 independent experiments. Scale bar = 2μm.
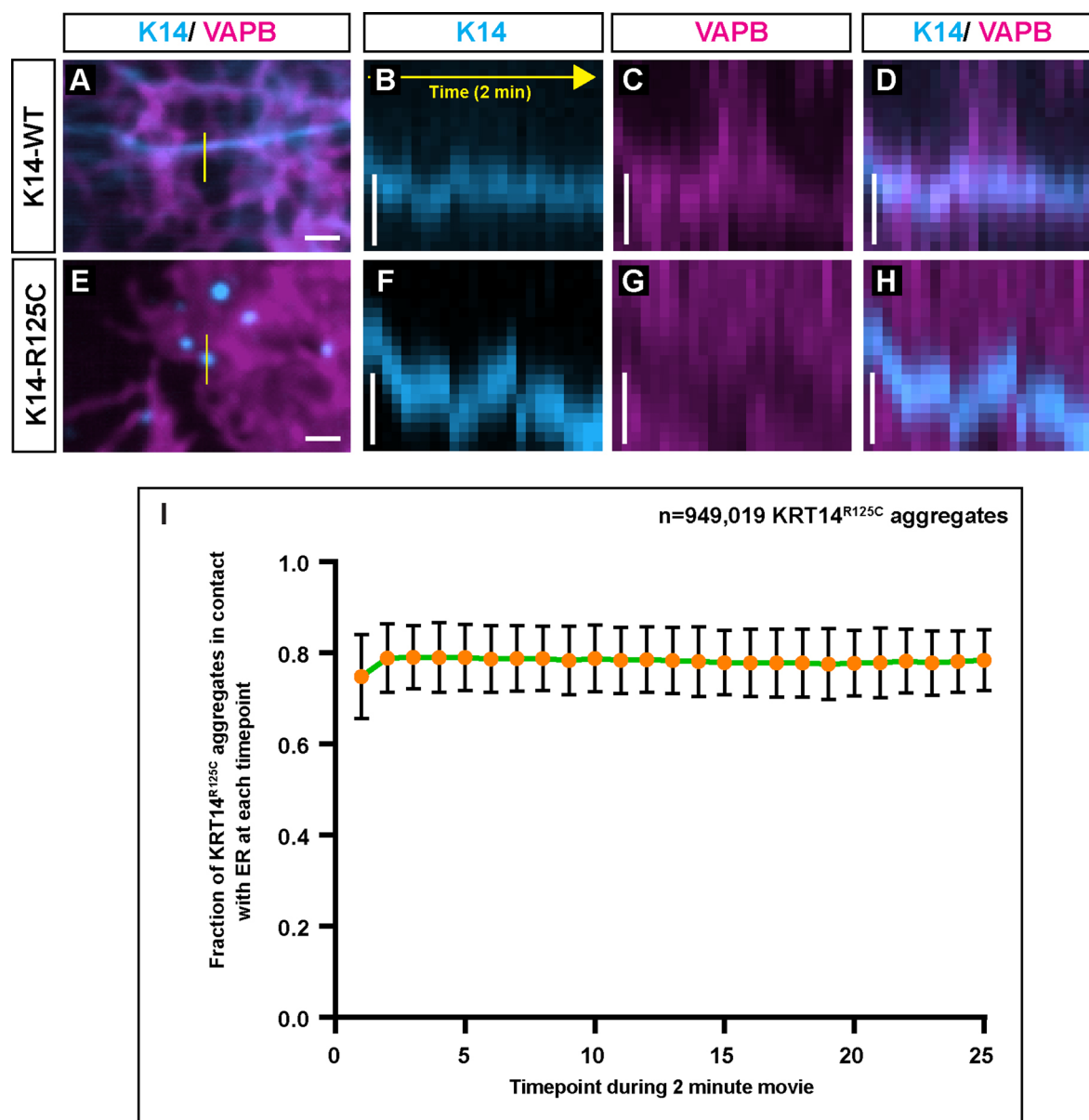
Extended Data Fig. 10 | Keratin filaments and aggregates are stably tethered to ER membranes. (a) Snapshot of an A431 cell expressing mNeonGreen-KRT14[WT] (blue) and mApple-VAPB (magenta) showing ER tubules along keratin filaments (Images are representative of n = 3 independent experiments). Solid yellow line indicates position of kymograph in B-D. Scale bar = 1μm. **(b-d)** Kymograph of yellow line in A revealing stable ER-keratin interaction over a 2-minute time course. Scale bar = 500 nm. **(e)** Snapshot of an A431 cell expressing mNeonGreen-KRT14[R125C] (blue) and mApple-VAPB (magenta) showing ER sheets surrounding KRT14[R125C] aggregates (Images are representative of n = 3 independent experiments). Solid yellow line indicates position of kymograph in F-H. Scale bar = 1μm. **(f–h)** Kymograph of yellow line in E revealing stable ER-keratin interactions over a 2-minute time course. Scale bar = 500 nm. **(i)** Graph depicting the fraction of KRT14[R125C] aggregates colocalizing with ER at each timepoint during a 25 timepoint/2-minute time course. Data are represented as mean ± s.d.; n indicates total number of KRT14[R125C] aggregates analyzed from three independent experiments. Source numerical data are available in source data.

nature portfolio

Corresponding author(s): Andrew P Kowalczyk

Last updated by author(s): *YYYY-MM-DD*

Reporting Summary

Nature Portfolio wishes to improve the reproducibility of the work that we publish. This form provides structure for consistency and transparency in reporting. For further information on Nature Portfolio policies, see our Editorial Policies and the Editorial Policy Checklist.

Statistics

For all statistical analyses, confirm that the following items are present in the figure legend, table legend, main text, or Methods section.

n/a	Confirmed	
☐	☒	The exact sample size (*n*) for each experimental group/condition, given as a discrete number and unit of measurement
☒	☐	A statement on whether measurements were taken from distinct samples or whether the same sample was measured repeatedly
☐	☒	The statistical test(s) used AND whether they are one- or two-sided *Only common tests should be described solely by name; describe more complex techniques in the Methods section.*
☒	☐	A description of all covariates tested
☐	☒	A description of any assumptions or corrections, such as tests of normality and adjustment for multiple comparisons
☐	☒	A full description of the statistical parameters including central tendency (e.g. means) or other basic estimates (e.g. regression coefficient) AND variation (e.g. standard deviation) or associated estimates of uncertainty (e.g. confidence intervals)
☐	☒	For null hypothesis testing, the test statistic (e.g. *F*, *t*, *r*) with confidence intervals, effect sizes, degrees of freedom and *P* value noted *Give P values as exact values whenever suitable.*
☒	☐	For Bayesian analysis, information on the choice of priors and Markov chain Monte Carlo settings
☒	☐	For hierarchical and complex designs, identification of the appropriate level for tests and full reporting of outcomes
☒	☐	Estimates of effect sizes (e.g. Cohen's *d*, Pearson's *r*), indicating how they were calculated

Our web collection on statistics for biologists contains articles on many of the points above.

Software and code

Policy information about availability of computer code

Data collection	Live-cell fluorescence microscopy was performed using a Nikon Ti2-E equipped with a Yokogawa CSU-X1 spinning disk unit, and the acquisition was controlled with NIS-Elements v5.30.02, v5.30.04, and v5.30.06. Transmission electron microscopy was done using a FEI Tecnai G2 or Talos transmission electron microscopes operated at 120 kV. Cryo-SIM and FIB-SEM imaging was performed with custom-built microscopes within the Advanced Imaging Center at Janelia Research Campus, a facility jointly supported by the Gordon and Betty Moore Foundation and the Howard Hughes Medical Institute. RT-PCR was performed using a Light Cycler 480 (Roche). Chemiluminescent blots were imaged with a ChemiDoc MP Imaging System (Bio-Rad).
Data analysis	Fiji (ImageJ v1.53t) was used for densitometric analysis of chemiluminescent blots. Alignment and reconstruction of the FIB-SEM images was performed using a pipeline based on render web services (github.com/saalfeldlab/render). Following alignment, the volumes were flattened using a spline along the z dimension based on key points that were interactively set in BigDataViewer. Automatic ER, mitochondria, and plasma membrane segmentation in FIB-SEM datasets from COSEM used previously described networks from https://github.com/janelia-cosem/heinrich-2021a. Manual validation to choose the optimal network iterations used a Fiji plugin https://github.com/janelia-cosem/Fiji_COSEM_Predictions_Evaluation. Fiji (ImageJ v1.53t) was used for cropping/reslicing FIB-SEM datasets before using Microscopy Image Browser (v2.83) and DragonFly (v2022.2) for further processing, proofreading, and analysis. For CLEM registration, mitochondria segmentation of the FIB-SEM dataset were downsampled and coarsely aligned using BigDataViewer before Gaussian smoothing in Fiji. Elastix was then used for registering the smoothed EM-mitochondria predictions with the fluorescence mitochondria signal. Code for the elastix workflow can be found at https://github.com/saalfeldlab/template-building. ImageJ macros for processing/analyzing the live-cell spinning disk confocal datasets can be found at https://github.com/KowalczykLab/

Desmosome-ER/.
For denoising of live-cell spinning disk confocal datasets, we used Noise2Void (Python: v0.2.1, Fiji: https://github.com/CSBDeep/CSBDeep_fiji) and 3DRCAN (https://github.com/AiviaCommunity/3D-RCAN).
Quantitative RT-PCR analysis was performed using Microsoft Excel (v2303).
Statistical testing was performed using R (v4.2.3) or Graphpad Prism 8.
The Python packages seaborn (v0.12.0) and matplotlib (3.7.1) were used for generating some plots.

For manuscripts utilizing custom algorithms or software that are central to the research but not yet described in published literature, software must be made available to editors and reviewers. We strongly encourage code deposition in a community repository (e.g. GitHub). See the Nature Portfolio guidelines for submitting code & software for further information.

Data

Policy information about availability of data

All manuscripts must include a data availability statement. This statement should provide the following information, where applicable:
  - Accession codes, unique identifiers, or web links for publicly available datasets
  - A description of any restrictions on data availability
  - For clinical datasets or third party data, please ensure that the statement adheres to our policy

All macros and plasmid maps are available at https://doi.org/10.5281/zenodo.6800360.
FIB-SEM datasets are hosted on: https://www.openorganelle.org/datasets/aic_desmosome-2 and https://www.openorganelle.org/datasets/aic_desmosome-3.
Other imaging source data, including spinning disk confocal microscopy data, is hosted on ScholarSphere (doi:10.26207/53vq-g344).
Source data for graphs and western blots are provided with this paper.
All other data supporting the findings of this study are available from the corresponding author on reasonable request.

Human research participants

Policy information about studies involving human research participants and Sex and Gender in Research.

Reporting on sex and gender	No human participants were involved with this study.
Population characteristics	Samples were discarded and de-identified.
Recruitment	N/A.
Ethics oversight	Experiments described in this manuscript utilized discarded and/or de-identified human skin and pemphigus patient samples. These experiments were reviewed and determined to be "not human subjects research" by the Pennsylvania State University Office for Research Protections (PSU IRB STUDY00021792).

Note that full information on the approval of the study protocol must also be provided in the manuscript.

Field-specific reporting

Please select the one below that is the best fit for your research. If you are not sure, read the appropriate sections before making your selection.

☒ Life sciences   ☐ Behavioural & social sciences   ☐ Ecological, evolutionary & environmental sciences

For a reference copy of the document with all sections, see nature.com/documents/nr-reporting-summary-flat.pdf

Life sciences study design

All studies must disclose on these points even when the disclosure is negative.

Sample size	Sample sizes are indicated in figure captions. No predetermined tests were performed to calculate sample size.

The sample sizes for live-cell imaging experiments were chosen based on past experience in the lab and previous studies (PMID: 31243490, 32399559, 33554435, 25416943). The cells used for live-cell experiments were stable immortalized/ transformed cell lines that were not clonally selected and therefore represented a population.

Sample sizes for FIB-SEM datasets were limited by acquisition time, sample preparation, and time for accurate and precise segmentation. In total, the two uncropped FIB-SEM datasets required 12 days of continuous FIB-SEM scope time. Sample tearing from the resin embedding step meant that some desmosomes had to be excluded from analyses concerning distances to other structures. Although both datasets came from the same coverslip, they focused on two different cell-cell contacts and their FIB-SEM acquisition parameters differed to trade dataset volume for better resolution. Only the 4x4x4 nm^3 dataset had sufficient resolution for resolving microtubules, and analysis requirements mandated manual annotation.

The 27 and 6 desmosomes in the 8x8x8 nm^3 and 4x4x4 nm^3 datasets, respectively, showed that ER is close to desmosomes on both sides, in contrast to other organelles like endosomes and microtubules. The findings from these two datasets show ER and keratin contacting at desmosomes and ER contacting the desmosome outer dense plaque, and have the resolution to measure the distance of ER from |

desmosomes. These high-resolution volume electron microscopy datasets complement our live-cell fluorescence confocal imaging where we can instead study dynamics of ER and keratin.

Data exclusions	Some desmosomes in the FIB-SEM datasets were excluded because of sample tearing or because only part of the desmosome was contained within the cropped datasets. Live-cell datasets were excluded if there was significant sample drift. For calcium switch experiments, datasets were excluded if two or more cells did not form cell-cell contacts.
Replication	All experiments were repeated at least three times, unless specified otherwise in the legends, and similar results were obtained in all replicates. CLEM was performed on two ROIs within the same coverslip, but acquisition parameters differed in resolution. Both datasets showed similar results. TEM was performed on cultured human cells and two different rat organ systems (skin and gut tissue). Western blot was repeated twice and similar results were obtained. DMSO control for thapsigargin and nocodazole treatment experiments (Fig. 5, Extended Data Fig. 7, Extended Data Fig. 9) were performed at least twice. Our results are consistent with previously published thapsigargin experiments.
Randomization	For live-cell imaging experiments, cells expressing fluorescent constructs were seeded into wells and image fields were selected based on 2 criteria: 1. Two or more adjacent cells expressing the fluorescent constructs were in the same field, and 2. adjacent cells had similar fluorescence intensity levels. Covariates were controlled by maintaining all samples in the same growth conditions on the same dish (in different wells), until addition of drug or DMSO. For the CLEM experiments, regions were chosen for FIB-SEM acquisition using the results of Cryo-SIM imaging with the following conditions for all cells within the regions of interest: 1. Similar expression levels of mApple-VAPB and DP-EGFP, and 2. Healthy/normal morphology. Further cropping of FIB-SEM datasets was necessary for analysis due to computer hardware constraints and segmentation requirements. The cropped regions for analysis were chosen because they contained desmosomes without being greatly impacted by sample tearing.
Blinding	The Investigators were not blinded to allocation during experiments and outcome assessment. Blinding was not possible since data collection and analysis were done by the same investigator.

Reporting for specific materials, systems and methods

We require information from authors about some types of materials, experimental systems and methods used in many studies. Here, indicate whether each material, system or method listed is relevant to your study. If you are not sure if a list item applies to your research, read the appropriate section before selecting a response.

Materials & experimental systems

n/a	Involved in the study
☐	☒ Antibodies
☐	☒ Eukaryotic cell lines
☒	☐ Palaeontology and archaeology
☐	☒ Animals and other organisms
☒	☐ Clinical data
☒	☐ Dual use research of concern

Methods

n/a	Involved in the study
☒	☐ ChIP-seq
☒	☐ Flow cytometry
☒	☐ MRI-based neuroimaging

Antibodies

Antibodies used	Mouse monoclonal anti-desmoglein3 (AK23). Pemphigus vulgaris Abs. The following antibodies and dilutions were used for western blot: 1:1000 rabbit anti-desmoplakin (A303-356A; Bethyl Laboratories), 1:1000 rabbit anti-VAPB (PA5-53023; Invitrogen), and 1:60,000 rabbit anti-GAPDH (10494-1-AP; Proteintech). Secondary antibodies used were: 1:3000 Goat Anti-Rabbit IgG (H+L) Horseradish peroxidase conjugate (170-6515; Bio-Rad).
Validation	The AK23 antibody has been validated in previous literature (Tsunoda et al. 2003, and later studies). Pemphigus vulgaris Abs have been validated in (Saito et al., 2012, Stahley et al., 2016). Antibodies for western blotting were selected based on their routine use by our lab or in literature. Rabbit anti-DP (A303-356A; Bethyl Laboratories) antibody used has been validated by our lab in cell lines that have dysfunctional desmosomes by indirect immunofluorescence and western blot of cell lysates. Rabbit anti-VAPB antibody (PA5-53023; Invitrogen) has been validated by the manufacturer and our lab based on protein localization obtained from indirect immunofluorescence microscopy in fixed cells, as well as in VAPB knockdown cell lines. Rabbit anti-GAPDH antibody (10494-1-AP; Proteintech) was validated by the manufacturer. Goat Anti-Rabbit IgG (H+L) Horseradish peroxidase conjugate (170-6515; Bio-Rad) secondary antibody was validated by western blot of cell lysates.

Eukaryotic cell lines

Cell line source(s)	A431 parental cells were provided by Dr. James Wahl, University of Nebraska Medical Center, Lincoln, NE. HaCaT keratinocytes were provided by Dr. Kathleen Green, Northwestern University, Chicago, IL. Normal Human Epidermal Keratinocytes were isolated from neonatal foreskin (Calkins et al., 2006). HEK-293FT cells were provided by Dr. James Zheng, Emory University, Atlanta, GA.
Authentication	We routinely characterize A431 and HaCaT cells for expression of epithelial cell marker proteins, which further validates their identity. HEK-293FT cells are validated through morphology and weak adherence to the substrate, and generation of lentivirus particles. Primary human keratinocytes are also used and these cells are also routinely monitored for expression of keratinocyte marker proteins (such as keratins, desmosomal proteins, cadherins). DSG2-null A431 cell lines were authenticated by antibody labelling.
Mycoplasma contamination	Cell lines were not tested for mycoplasma contamination.
Commonly misidentified lines (See ICLAC register)	No commonly misidentified cell lines were used in this study.

Animals and other research organisms

Laboratory animals	Sprague Dawley rats.
Wild animals	The study did not involve wild animals.
Reporting on sex	Sex of the animals is unknown.
Field-collected samples	The study did not involve field-collected samples.
Ethics oversight	Tissue samples were excised from Sprague Dawley rats used in the following two studies according to protocols approved by Animal Care Committees at the respective institutions: NIH/NIAAA R01 AA022460 to Joanne Weinberg et al., Animal care protocol AUP 21-02-01 to Charlis Raineki, Brock University, Canada. RGPIN-2018-03727 to A. Wayne Vogl, Animal care protocol A20-0076 to AWV, University of British Columbia, Canada.

Note that full information on the approval of the study protocol must also be provided in the manuscript.